



**HOLES:
IONOSPHERIC SCINTILLATION
GPS
AND IMPUTATION**

THESIS

Robert A. Steenburgh, Senior Master Sergeant, USAF

AFIT/GAP/ENP/07-06

**DEPARTMENT OF THE AIR FORCE
AIR UNIVERSITY**

AIR FORCE INSTITUTE OF TECHNOLOGY

Wright-Patterson Air Force Base, Ohio

APPROVED FOR PUBLIC RELEASE; DISTRIBUTION UNLIMITED.

The views expressed in this thesis are those of the author and do not reflect the official policy or position of the United States Air Force, Department of Defense, or the United States Government.

AFIT/GAP/ENP/07-06

HOLES:
IONOSPHERIC SCINTILLATION
GPS
AND IMPUTATION

THESIS

Presented to the Faculty
Department of Engineering Physics
Graduate School of Engineering and Management
Air Force Institute of Technology
Air University
Air Education and Training Command
In Partial Fulfillment of the Requirements for the
Degree of Master of Science in Applied Physics

Robert A. Steenburgh, AAS,BS
Senior Master Sergeant, USAF

March 2007

APPROVED FOR PUBLIC RELEASE; DISTRIBUTION UNLIMITED.

HOLES: IONOSPHERIC SCINTILLATION GPS AND IMPUTATION

Robert A. Steenburgh, AAS,BS
Senior Master Sergeant, USAF

Approved:

/signed/

21 Mar 2007

Christopher Smithtro (Chairman)

Date

/signed/

21 Mar 2007

William Bailey (Member)

Date

/signed/

21 Mar 2007

David Kaziska (Member)

Date

Abstract

Ionospheric scintillation of GPS signals threatens navigation and military operations by degrading performance or making GPS unavailable. Scintillation is particularly active, although not limited to, a belt encircling the earth within $\pm 20^\circ$ of the geomagnetic equator. This belt also hosted roughly half of the completed U.S. military operations in the last decade. We examined scintillation data from Ascension Island, U.K. and Ancon, Peru, in the Atlantic & Americas longitudinal sector as well as data from Parepare, Indonesia and Marak Parak, Malaysia in the Pacific longitudinal sector. From these data, we calculate percent probability of occurrence of scintillation at various intensities described by the S_4 index. Additionally, we determine Dilution of Precision at one minute resolution. Diurnal, seasonal and solar cycle characteristics are examined. Latitudinal and longitudinal comparisons are made. Our findings are consistent with previous research. Unlike previous research, however, we attempt to replace, or impute, missing S_4 values in order to better capture the extent of scintillation. In doing so, we study data gaps, or holes, and characterize them.

Acknowledgements

I was privileged to work with my advisor, Maj Chris Smithtro, and the members of my committee, Dr William Bailey and Maj Dave Kaziska. They transformed an old meteorologist into a new physicist, not an easy task. They introduced me to new worlds, taught me to keep asking questions and yet never lost patience with me. Dr Keith Groves of the Air Force Research Laboratory and Ron Caton of Atmospheric and Environmental Research provided data and direction. Dr John Raquet guided me through the intricacies of GPS navigation and provided `Matlab`[®] scripts that enabled me to make HDOP calculations. Dr Chuck Lekeas wrote FORTRAN routines to process and format the data saving me weeks of development time. Jeff Sitler kept our computational resources well tuned and our snack-bar well stocked.

I owe a special debt of gratitude to my colleague 1Lt Joshua Werner. He made the journey from meteorologist to physicist with me and it was good to have a companion along the way. He gave me good counsel and kept me from making careless mistakes. Additionally, Capt Brett Spangler and Capt Shaun Easely provided valuable feedback and insight, enabling me to approach this topic from different angles.

In the course of this research, the faculty in both the Physics and Mathematics Departments helped me grow as a scientist, military member, and human being. I was honored to be among these good people. The United States and its Air Force reap the fruits of their labor.

Robert A. Steenburgh

Table of Contents

	Page
Abstract	iv
Acknowledgements	v
List of Figures	viii
List of Tables	ix
List of Abbreviations	x
 I. Introduction	 1
1.1 Overview	1
1.2 The Research	3
1.3 This Work	4
 II. Background	 5
2.1 The Global Positioning System	5
2.1.1 Determining Location	5
2.1.2 Coordinate Systems and Transformations	7
2.1.3 Sources of Error	8
2.1.4 Dilution of Precision	9
2.1.5 Characteristics of GPS Transmissions	11
2.2 The Ionosphere	12
2.2.1 Characteristics of the Ionosphere	12
2.2.2 Earth's Magnetic Field Interacts with Ionospheric Plasma	13
2.3 Scintillation: A Consequence of Ionospheric Irregularities	22
2.3.1 Wave Propagation in Plasma	22
2.3.2 Definition, Characteristics and Models	23
2.3.3 Research on Scintillation and its Impacts on GPS . . .	29
 III. Method	 32
3.1 Data Description	32
3.2 Data Preparation and Irregularities	34
3.3 Data Processing	48

	Page
IV. Results and Analysis	53
4.1 Solar Cycle Comparison	54
4.2 Seasonal Comparison	60
4.3 Diurnal Comparison	63
4.4 Annual Horizontal Dilution of Precision (HDOP) Summaries .	63
4.5 Imputation Performance	66
4.6 Summary	71
V. Summary and Conclusions	74
5.1 Future Work	75
Appendix A. Raw Data File Example	77
Appendix B. Z-Test on Means	80
Bibliography	86
Vita	89

List of Figures

Figure		Page
2.1	Electron Density Profile with Ionospheric Layers	14
2.2	Appleton Anomaly	16
2.3	Rayleigh Taylor Instability	17
2.4	Perturbation Growth	18
2.5	Scintillation	25
2.6	Phase Screen Illustration	25
2.7	Nakagaim-m Probability Density Function	28
3.1	SCINDA Sites and Years Operating	33
3.2	Satellite Outage Duration	37
3.3	Day of Year vs Outage Duration	38
3.4	Elevation Angle vs Outage Duration	39
3.5	Satellite Elevation Near Mask	39
3.6	Elevation Angle Distribution Before and After Outage	41
3.7	Day of Year vs Outage Duration excluding outages below 20°	43
3.8	Maximum S_4 vs. Variance S_4 – Atlantic/Americas Sector	45
3.9	Large Scale Data Gaps	49
4.1	Ascension 2001, Week 11, Percentage of Satellites with $S_4 > 0.5$	55
4.2	Ascension 2001, Week 11, Percentage of Satellites with $S_4 > 0.3$ (a) and $S_4 > 0.8$ (b)	56
4.3	2001 Summary for Ascension, Ratio of satellites with $S_4 > 0.3$ to all available, 50 th , 75 th , and 95 th Percentile	57
4.4	Solar Cycle Comparison: Ascension, Ancon, Parepare and Marak Parak	58
4.5	Solar Cycle Comparison Parepare	59
4.6	Seasonal Comparison	61
4.7	Seasonal Comparison for Ascension	62
4.8	Diurnal Comparison, Ascension, Ancon, Parepare, and Marak Parak . .	64
4.9	Diurnal Comparison, Parepare week 13, 2000	65
4.10	HDOP Comparison	67
4.11	HDOP Relative Difference	68
4.12	Difference between Imputed and Raw data at Ascension in 2001	70
4.13	Difference between Imputed and Raw data at Ascension in 2001 - new thresholds	72

List of Tables

Table		Page
2.1	Ionospheric Characteristics	13
2.2	Temporal and Spatial Characteristics of Equatorial Plasma Bubbles & Scintillation	21
3.1	SCINDA Site Characteristics	32
3.2	Long Duration Outages at Marak Parak, 2000	44
3.3	Correlation Coefficients for Max vs $\sigma_{S_4}^2$	44
3.4	Fraction of Satellites Involved in Outages & Percentage of Outages by Maximum S_4	46
3.5	Summary Plot Data Combinations	52
1	Results of Z-Test on Means	81

List of Abbreviations

Abbreviation	Page
GPS	Global Positioning System 1
EM	Electromagnetic 2
TEC	Total Electron Content 2
HDOP	Horizontal Dilution of Precision 3
ECEF	Earth-Centered Earth-Fixed 7
LLA	Latitude, Longitude, Altitude 7
ENU	East, North, Up 7
WGS-84	World Geodetic System 1984 7
URE	User Equivalent Range Error 9
DOP	Dilution of Precision 9
GDOP	Geometric Dilution of Precision 11
PRN	Pseudo-Random Noise 11
C/A Code	Coarse-Acquisition Code 11
P-Code	Precise Code 11
PRE	Pre-Reversal Enhancement 15
EPBs	Equatorial Plasma Bubbles 15
ESF	Equatorial Spread-F 20
TEC	Total Electron Content 23
SCINDA	Scintillation Decision Aid 29
C/NOFS	Communication/Navigation Outage Forecasting System 29
WBMOD	WideBand MOdel 30
AFRL	The Air Force Research Laboratory 32
IGRF10	International Geomagnetic Reference Field 32
MNAR	Missing Not At Random 35

HOLES: IONOSPHERIC SCINTILLATION GPS AND IMPUTATION

I. Introduction

“Wherever you go, there you are.”

1.1 Overview

Over the centuries various tools and techniques have been developed specifically to answer the question, where are we? Accurate position information is critical for a myriad of human endeavors, from travel and trade to disaster relief and defense. This fact has been reflected in the refinement of navigational tools and techniques over the centuries. Increasing navigational precision and accuracy has been paralleled by, and to some degree driven by, a concurrent increase in the lethality of weaponry.

The United States military has publicly promoted the precision of its weaponry. Phrases like “surgical strike” and “smart bomb” have become part of the popular lexicon. Understandably, political leaders and the general public have increased expectations, amplifying the political consequences of collateral casualties from a misplaced missile strike or blundered bombing. Natural phenomena that degrade targeting accuracy, therefore, merit understanding. This is the thrust of our research. In particular, we examined the impact of a phenomenon called ionospheric scintillation on the availability and precision of information from the Global Positioning System (GPS). We found that depending on the temporal and spatial circumstances, the impact of scintillation can range from the benign to catastrophic, from virtually no discernible impact to a total system outage for the affected region.

Since its inception in the early 1970s, the GPS has become the cornerstone of our military’s ability to effectively navigate and target. Twenty four GPS satellites orbit the Earth at at 20,200 km. Using signals from as few as, but no less than four of these satellites, a receiver on the ground can calculate the transit time of the electromagnetic (EM) signals from the satellites, and with some adjustment for clock-error, generate position information. Today, GPS receivers can be found not only in weapon systems, but also in commercial vessels, automobiles, and mobile telephones.

Before reaching a receiver, however, the GPS transmissions must pass through the Earth’s ionosphere. This region of plasma envelops the Earth from beyond 1000 km down to approximately 60 km and is formed primarily through photo-ionization, but subject to other chemical and kinematic processes [*Schunk and Nagy, 2000*]. The plasma refracts the GPS transmission, delaying the arrival of the carrier wave. Ionospheric path delay occurs in a manner that is reasonably predicted and ameliorated; in fact, it can be exploited to estimate the integrated number density of electrons in a column with a one m² cross sectional area extending from the receiver to the satellite; the Total Electron Content (TEC). Scintillation of the signal because of ionospheric irregularities, on the other hand, is less predictable and more difficult to contend with.

Although scintillation can occur anywhere over the Earth, certain regions are conducive to the phenomenon. One such region encircles the Earth within $\pm 20^\circ$ of the geomagnetic equator, forming a “scintillation belt” that encompasses approximately 1/3 of the Earth’s surface [*Schunk and Nagy, 2000*]. This region has also hosted roughly half of the completed United States military operations in the past decade, according to data culled from *globalsecurity.org*. Not surprisingly, receivers were deployed throughout the “scintillation belt” beginning in the 1990s to monitor ionospheric scintillation at GPS frequencies [*Groves et al., 1997*]. The confluence of these three factors provided both the opportunity and the impetus to study equatorial ionospheric scintillation and its impact on GPS.

1.2 The Research

The goal of our research was to determine the number and percentage of GPS satellites affected by various levels of scintillation. The amount of error associated with GPS measurements is, to a certain extent, a consequence of the number and position of the available GPS satellites, so we also examined the impact of scintillation on the horizontal dilution of precision, or HDOP. We examined data collected during solar minimum and maximum at four stations. This work is essentially a continuation of that begun by *Thomas et al.* [2001]. That research involved similar calculations, with the exception of HDOP, for stations in the Pacific during 1998-1999, prior to the solar maximum in 2001.

During severe scintillation, receivers can lose the signal from one or more satellites; civilian and military GPS users need to know about this phenomenon because navigation is threatened. Statistics that do not take into account this phenomena risk underestimating the magnitude of scintillation. Assuming that data are missing precisely because of severe scintillation, we could replace, or impute, the missing data with a proxy to indicate the severity. This is at best a gamble, and at worst, a serious distortion. However, if done carefully and the results used with caution, it can provide a more complete picture of the synoptic behavior of this phenomenon.

The imputation scheme we developed was able to produce realistic patterns of scintillation. Examination of imputation augmented statistics from Ancon, Peru; Ascension Island, U.K.; Parepare, Indonesia, and Marak Parak, Malaysia reflected seasonal, diurnal, solar-cycle, and spatial dependencies.

In order to create a reasonable imputation scheme, we had to learn as much as possible about the missing data events, or as we called them, holes or outages. The amount of missing data is typically small and therefore ignored. To our knowledge, this is the first research in which time was spent examining the outages. Amplitude scintillation is typically characterized by the ratio of the standard deviation of signal intensity to its mean, which is called the S_4 index. We found a strong correlation

between the maximum value of the S_4 index and the variance of S_4 prior to an outage. Outages usually lasted less than 10 min and longer duration outages were generally associated with low elevation satellites. These findings guided our design of an imputation scheme.

1.3 This Work

The remainder of this work is concerned with understanding the synoptic behavior of scintillation and quantifying its impacts on GPS. In Chapter II, the reader is acquainted with GPS, introduced to the ionosphere and finally, provided with background on scintillation and the research to date. Chapter III is concerned with the getting the numbers. We describe the techniques used to discriminate between the good and bad data, and fill in the missing data. Here we digress and examine the characteristics of holes. Chapter IV contains the results. The striking examples are here, demonstrating the temporal and spatial variations as well as pointing out the utility of imputation. Finally, Chapter V concludes with my ideas for continued exploration of scintillation using ground based observations collected by GPS receivers.

II. Background

THIS chapter provides background on GPS, the ionosphere and the interactions leading to scintillation. A discussion of scintillation and its impact on electromagnetic waves follows. We end with a survey of research to date on scintillation and its impacts on GPS.

2.1 *The Global Positioning System*

The first step toward exploring the effect of scintillation on GPS requires an understanding of GPS itself. As mentioned in the preceding chapter, a constellation of 24 operational GPS satellites surrounds the Earth at an altitude of 20,200 km, in six orbital planes, with an orbital period of 12 sidereal hours. As we imagine the satellites orbiting overhead, several questions come to mind. For instance, how are satellite signals used to determine location? What coordinate systems are used? The signals emitted by the GPS satellites are complex, carrying a great deal of information. Which ones were collected for this research? Additionally, errors from a variety of sources accumulate as signals travel from the satellites to a receiver and are processed; these must be accounted for. The errors, in turn, influence the precision of the location estimate. How are these related? Finally, satellite orbit data are available in varying degrees of accuracy. Which will be used for this research? Unless otherwise noted, the organization and content of this section was culled from course notes provided by J. Racquet (EENG 533, *Navigation Using the GPS*, course handouts, 2006).

2.1.1 Determining Location. One method of determining location involves transmitting a signal and recording the precise time the signal was sent from the transmitter and the precise time it arrives at a receiver. With knowledge of the signal's velocity through the transmission medium, the range can be extracted. For electromagnetic waves in a vacuum, ignoring relativistic effects and assuming a fixed transmitter and receiver, the distance to the transmitter to the receiver is given by $d = ct$ where c is the speed of light and t is the travel time for the signal to reach the receiver. At this point only the distance from a particular transmitter is known,

but not yet the location. Two additional transmitters are needed to produce a unique solution (location). With signals from all three transmitters providing the range to each, the relative position can be determined. The intersection of three circles, each centered on a transmitter with a radius equal to the calculated range, provides the position to the transmitters (for a two dimensional case). *This assumes perfect synchronization of all three transmitter clocks and the receiver clock.* This case can easily be extended to three dimensions by replacing the circles with spheres.

In practice, GPS receiver clocks are less accurate and not synchronized with the satellites, so clock error, δt , is introduced. This is the offset between the receiver clock and the satellite clock [Hofmann-Wellenhof et al., 2001]. The distance equation becomes

$$d = d + c\delta t \tag{2.1}$$

The distance is typically referred to as range, and range with clock error is called *pseudo-range*, denote by ρ . The consequence of clock error is to require a fourth satellite to accurately determine position. Returning to the three circles and introducing a fourth, the position is now at the center of a *fifth circle*, tangent to the other four. The radius of the fifth circle represents the Δd introduced above. Again, this can be extended to three dimensions.

Approaching the problem from another perspective, in order to know location in three dimensions, three coordinates, x , y , and z are required. With three unknowns, three versions of equation (2.1) are needed to solve for d , hence signals from three satellites. Having introduced a fourth unknown δt , four equations (and consequently four satellites) are necessary in order to produce a navigation solution. The resulting system of equations can be solved using methods described by Hofmann-Wellenhof et al. [2001, chap. 9].

Until now the discussion of pseudo-ranges to GPS satellites has taken place in a Cartesian reference frame centered on the user. In the long run however, the typical GPS user is not concerned with his or her position relative to a constellation of GPS

satellites, but rather his or her position with respect to Earth or locations on the Earth. Before moving further, therefore, three coordinate systems are introduced and discussed.

2.1.2 Coordinate Systems and Transformations. We are interested in three coordinate systems:

- Earth-Centered Earth-Fixed (ECEF)
- Geodetic or Latitude, Longitude, Altitude (LLA)
- Local or East, North, Up (ENU)

ECEF is a Cartesian reference frame centered on, and rotating with, the Earth. The LLA frame is based on the World Geodetic System 1984 WGS-84 ellipsoid, a global three-dimensional coordinate system used with geospatial data. In the simplest terms, the Earth is represented by a sphere that's "squashed" at the poles and bulges at the equator. The latitude (ϕ), longitude (λ) and altitude (m), with respect to the ellipsoid, determines position. Finally, the ENU frame is fixed to a point and oriented east, north and up. Later it will be necessary to rotate coordinates from an ECEF to a ENU framework. The ECEF coordinates must be adjusted with respect to the origin of the local level frame. Placing the satellites, as well as the receiver in a particular reference frame is essential because, as noted by *Hofmann-Wellenhof et al.* [2001, chap. 4], "For single receiver positioning, an orbital error is highly correlated with positional error." Information about a satellite's orbit, also known as ephemerides, is typically obtained from one of three sources, almanac files, broadcast ephemerides and precise ephemerides. Ephemerides allow a satellite to be placed in the desired reference frame. Of the three sources, almanac data are the most coarse with an uncertainty of some kilometers. It is updated weekly at a minimum and included in the broadcast satellite message [*Hofmann-Wellenhof et al.*, 2001]. Software used for this research ingested almanac data in YUMA format (one of two almanac formats) available from the United States Coast Guard Navigation

Center at <http://www.navcen.uscg.gov/gps/almanacs.htm>. Additional information regarding orbit data can be found in the resources mentioned earlier and also the encyclopedic volume by *Parkinson et al.* [1996].

On the topic of orbits, it is useful to note that the GPS ground track repeats every sidereal day, the time it takes the Earth to rotate once on its axis relative to inertial space (the stars). The sidereal day is shorter than the solar day by four minutes, so a given satellite will become available four minutes earlier each day. The effects of this behavior will become apparent on some of the figures in Chapter IV.

The alert reader may have noticed the surreptitious introduction of another error source, orbit error, in the preceding discussion. Rather than attempt to slip any more error sources in, we present a brief summary with attention focused on the sources most relevant to our research.

2.1.3 Sources of Error. Errors in addition to those introduced by the receiver and satellite can be appended to the pseudo-range equation 2.1, which becomes:

$$\rho = r + c \left(\delta t_u - \delta t_{sv} + \sum \delta t_{\text{other}} \right) \quad (2.2)$$

In equation 2.2 the δt term from 2.1 was expanded, accounting separately for the receiver (user) error δt_u , the satellite (space vehicle) error δt_{sv} and "all others" $\sum \delta t_{\text{other}}$. The last term is composed of errors introduced by:

- *Multipath*
- *the Ionosphere*
- the Troposphere
- Receiver Noise and Resolution Error
- Hardware
- Selective Availability

The italicized items indicate the error sources considered in this investigation. We will limit the discussion here to multipath, since the ionosphere contribution will be examined in detail in Section 2.2. When signals from a GPS satellite reach a receiver via multi(ple)-paths, this is multipath. Multipath can result from low satellite elevation and poor receiver and antenna siting with respect to buildings, terrain, etc. As noted by *Hofmann-Wellenhof et al.* [2001], in severe cases, low-elevation multipath can result in loss of a GPS signal. Less severe cases can result in measurement errors. Mitigation can be achieved by employing choke-ring type antennas with better gain, and by careful siting of the antenna. Since multipath can introduce errors and outages, researchers often apply a mask to exclude data from satellites below elevations up to 40° [*Thomas et al.*, 2004], although 15° seems common [see, e.g., *Datta-Barua et al.*, 2003]. For our research we applied a 15° mask to all the data.

The sum of the measurement errors listed above is called the User Equivalent Range Error (UERE) and can be multiplied by a factor called *dilution of precision* to obtain position error.

2.1.4 Dilution of Precision. Dilution of Precision (DOP) directly relates measurement errors to position errors. To arrive at DOP, we must begin with the pseudo-range equation (2.2) introduced earlier. Following a development of the DOP equation by J. Raquet (EENG 533, *Navigation Using the GPS*, course handouts, 2006), and also *Dempster* [2006], recall from Subsection 2.1.1 that four pseudo-range equations are necessary to solve for position. These equations can be expanded using a Taylor series, linearized, and solved through iterative techniques involving an approximate solution (i.e. guess). The linearized equations can be expressed as a matrix:

$$\Delta\rho = \mathbf{H}\Delta\mathbf{x} \text{ or} \tag{2.3}$$

$$\Delta\mathbf{x} = \mathbf{H}^{-1}\Delta\rho \tag{2.4}$$

where $\Delta \mathbf{x}$ is the vector of position and receiver clock corrections, $\Delta \rho$ is a vector of range error (i.e. difference between actual range and guess), and \mathbf{H} is the 4×4 matrix consisting of unit vectors (x, y, z) between the satellite and the guess position, plus a clock-error term. When more than four satellites are used, the system is overdetermined and can be solved using least-squares techniques. Equation (2.4) becomes:

$$\Delta \mathbf{x} = (\mathbf{H}^T \mathbf{H})^{-1} \mathbf{H}^T \Delta \rho \quad (2.5)$$

When two assumptions are made: that all measurements have the same variance, and the measurement errors are uncorrelated, we obtain through least-squares theory:

$$\mathbf{C}_x = (\mathbf{H}^T \mathbf{H})^{-1} \sigma_\rho^2 \quad (2.6)$$

where \mathbf{C}_x is the “covariance matrix of calculated position and clock error”, and σ_ρ^2 is the variance of the range measurement. If the \mathbf{H} matrix is transformed into local coordinates (ENU), the first term on the r.h.s. of Equation (2.6) becomes:

$$(\mathbf{H}^{G^T} \mathbf{H}^G)^{-1} = \begin{bmatrix} D_{11} & D_{12} & D_{13} & D_{14} \\ D_{21} & D_{22} & D_{23} & D_{24} \\ D_{31} & D_{32} & D_{33} & D_{34} \\ D_{41} & D_{42} & D_{43} & D_{44} \end{bmatrix} \quad (2.7)$$

where D_{ij} are in the local (geodetic) coordinate frame, indicated by the G (geodetic) superscript. This is the DOP matrix, and it directly relates position errors to measurement errors as we noted in the beginning of this section.

DOP can be thought as being inversely proportional to the volume of a body:

... This body is formed by the intersection of the [four] site-satellite vectors with the unit sphere centered at the observing site. The larger the volume of this body, the better the satellite geometry. Since good geometry should mirror a low DOP value, the reciprocal value of the volume of the geometric body is proportional to DOP. The critical configuration is

given when the body degenerates to a plane. [*Hofmann-Wellenhof et al.*, 2001]

DOP variants can then be extracted from the matrix. Geometric DOP, or GDOP is the square root of the trace of matrix (2.7). As noted by J. Raquet (EENG 533, *Navigation Using the GPS*, course handouts, 2006), the key relationship is

$$\text{GDOP} \times \sigma_{\text{UERE}} = \sqrt{\sigma_e^2 + \sigma_n^2 + \sigma_u^2 + \sigma_{\delta t_u}^2}, \quad (2.8)$$

which “relates UERE with the RSS (root square sum) of the errors.” We mentioned in Chapter I that our research is concerned with HDOP, the Horizontal Dilution of Precision, which is defined as:

$$\text{HDOP} = \sqrt{D_{11} + D_{22}}. \quad (2.9)$$

In practice, a DOP value of one is perfect, 10 is generally considered fair-poor, although the relative badness depends on the particular circumstances. The ionosphere influences DOP by degrading or obliterating GPS transmissions, thereby reducing the number of satellites which are available for a navigation solution. In order to understand how and why the ionosphere affects GPS transmissions, we need to know something about those transmissions.

2.1.5 Characteristics of GPS Transmissions. GPS transmits right-hand circularly polarized waves on two carrier frequencies, designated L1 and L2, at 1574.42 MHz and 1227.6 MHz respectively. The corresponding wavelengths are 19.03 cm for L1 and 24.42 cm for L2. The carriers are modulated by Pseudo-Random Noise (PRN) codes, of which there are two types, Coarse-Acquisition (C/A Code) code and Precise (P-Code) code. The C/A code is modulated on L1 only and is available to civilian users, while the P code appears on both L1 and L2, and although unclassified, is not typically transmitted. Instead, the P code is encrypted with a classified encryption key and called Y code, or P(Y) code. Each satellite is assigned its own PRN code,

although a particular PRN can be reassigned to another satellite. The PRN codes are identified by an integer in the range of 1 to 32, and the satellites are often referred to by their PRN. In addition to the PRN codes, the carrier is also modulated with a navigation message. This research was confined to reception of L1, C/A code only. Much can happen to the signal once it leaves the satellite, particularly as it travels through the ionosphere, the subject of the next section.

2.2 *The Ionosphere*

Becoming acquainted with the ionosphere is the next step toward understanding scintillation effects on GPS. In the preceding section, the Earth's ionosphere was mentioned as a source of error in GPS location estimates. We begin this section by introducing the structure and characteristics of the ionosphere. A description of the effect of Earth's magnetic field on the ionosphere follows. We conclude with a discussion of the interaction of EM waves with ionospheric plasma.

2.2.1 Characteristics of the Ionosphere. Earth's ionosphere forms in response to the interaction of energy from the sun with neutral atmospheric constituents. Chemical, electrodynamic, kinematic and mechanical processes are all at work at various latitudes and altitudes and within the ionosphere. The ionosphere can be stratified according to the processes (e.g. photochemical, transport) products (e.g. species) or phenomena (e.g. reflection of EM energy, density peaks). Characteristics of the ionosphere are shown given Table 2.1.

Table 2.1 shows the primary processes in the D, E, and F₁ regions are photochemical (including photo-ionization, recombination, charge exchange, etc), while a transition to transport dominance occurs within the F₂ layer. The Topside ionosphere is dominated by transport mechanisms, including ambipolar diffusion as well as gravitational, $\mathbf{E} \times \mathbf{B}$, and neutral wind drifts. Figure 2.1 is a modeled electron density profile with ionospheric layers from course notes, PH2514, Naval Postgraduate School, R.C. Olsen, 2003; details are included in the caption. Profiles are given

Table 2.1: A summary of mid and low-latitude ionospheric layers and characteristics summarized from [Schunk and Nagy, 2000]. Note the transition to transport that occurs in the upper F₂ layer. This will be important later when discussing the movement of plasma in the equatorial ionosphere.

Ionospheric Layers and Characteristics				
Layer	Height km	Dominant Process	Energy λ	Dominant Species
D	60–100	Photochemical	UV & X-ray	\pm ions and “water cluster” ions
E	100–150	Photochemical	EUV	$\text{NO}^+ \text{O}_2^+ \text{N}_2^+$
F ₁	150–250	Photochemical	EUV	O^+
F ₂	250–300 ^a	Photochemical– Transport	EUV	O^+
Topside Iono- sphere	>300	Transport (Diffusion, Drifts)	EUV	O^+

^aHeight of Electron Density Peak

for both day (solid) and night (dashed) as well as for solar maximum (right profile) and solar minimum (left profile). Notice how the layers decay to varying degrees at night in the absence of photo-ionization. The F₁ layer erodes entirely, while the E and F₂ regions remain, sustained by transport and slow recombination, respectively. Additionally, note the increase in electron density during solar maximum.

2.2.2 Earth’s Magnetic Field Interacts with Ionospheric Plasma. The seeds of scintillation are planted in the E-region of the ionosphere. Here, tidal winds drive an eastward dynamo current in the sunlit hemisphere [Kelley, 1989, chap. 3]. The resulting eastward electric field is perpendicular to the geomagnetic field lines, which in turn are virtually horizontal at the geomagnetic equator. Referring to Figure 2.2 [de La Beaujardiere et al., 2004] (looking east), the $\mathbf{E} \times \mathbf{B}$ drift drives the plasma upward. The plasma then diffuses along B field lines under the influence of gravity, \mathbf{g}_{\parallel} , and pressure gradients, $\nabla_{\parallel \mathbf{P}_1}$, as shown on the left and right sides of Figure 2.2. It accumulates $\approx 15\text{--}20^\circ$ north and south of the dip-equator. This phenomena is called the *Equatorial Fountain*. The accumulation of plasma poleward of

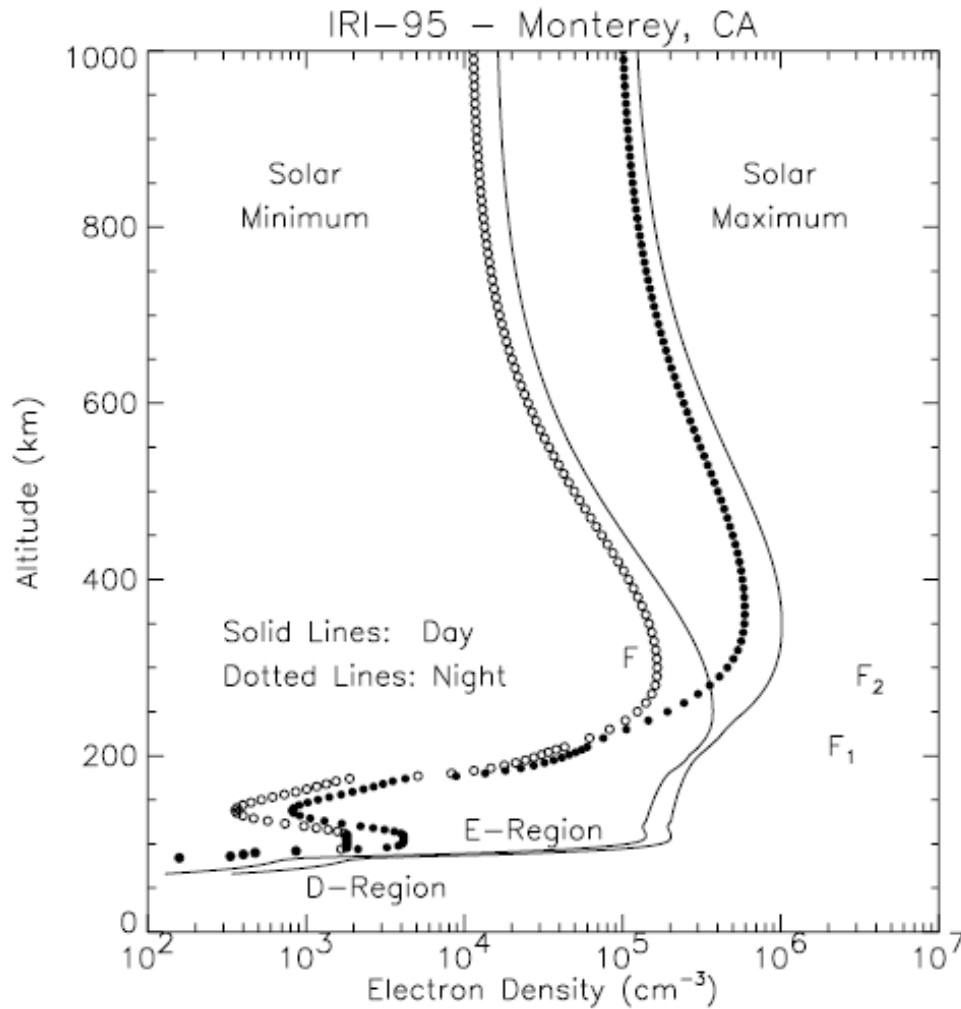


Figure 2.1: Electron Density Profile with Ionospheric Layers from course notes, PH2514, Naval Postgraduate School, R.C. Olsen, 2003. “The International Reference Ionosphere 1995 (IRI-95) model was run for the location of Monterey, CA (geographic latitude = 36.5, geographic longitude = 238), for July 4, 1989 (solar maximum) and July 4, 1995 (solar minimum). Calculations were done at 0LT (local midnight), and 12 LT (local noon)” Notice how the F₁ layer vanishes almost entirely during the night.

the geomagnetic equator is known as the *Appleton Anomaly* and the locations are labeled Ionization Crests in Figure 2.2. A meridional neutral wind, $\mathbf{V}_{n\parallel}$, that blows from the winter to summer hemisphere causes plasma in the summer hemisphere to be forced upward. Conversely, a downward drift occurs in the winter hemisphere thus the Appleton Anomaly is asymmetric across the equator. Figure 2.2 depicts neutral wind but not the resulting asymmetry.

The processes described above and illustrated in Figure 2.2 are confined to the daylight hemisphere. As Earth rotates into darkness, dramatic changes take place which can lead, ultimately, to scintillation. At the boundary between day and night (the terminator), the eastward electric field increases in response to increasing neutral winds [*Schunk and Nagy, 2000*] and “polarization charges within conductivity gradients at the terminator” [*de La Beaujardiere et al., 2004*] before becoming westerly. The upward $\mathbf{E} \times \mathbf{B}$ drift intensifies, raising the F layer. This is called the *Pre-Reversal Enhancement*(PRE). As darkness falls, photo-ionization ceases and the F region is quickly eroded from below as recombination takes place. The combination of lift and bottom-side erosion results in steep upward density gradient forces at the base of the F layer, directly opposed by gravity. This configuration is characterized by Rayleigh-Taylor Instability, in which a heavier fluid is supported by a lighter fluid. If perturbed, the fluid turns over, as illustrated in Figure 2.3, creating low-density structures (often referred to as bubbles) that rise through the denser fluid. In the equatorial ionosphere, they are known as Equatorial Plasma Bubbles (EPBs) although their shape more closely resembles elongated tubes.

Figure 2.4 illustrates perturbation growth in two dimensions. The F-region density gradient arising from the pre-reversal enhancement of the eastward electric field is modeled by a step-function. The magnetic field is directed into the page (looking north), gravity is directed downward and the density gradient is opposite gravity. A sinusoidal perturbation is imposed on this arrangement. Assuming the plasma is virtually collisionless, gravitational drift results in a current $J = n M \mathbf{g} \times \mathbf{B} / B^2$ which is directed eastward as shown on the left of Figure 2.4. Charges accumulate at the

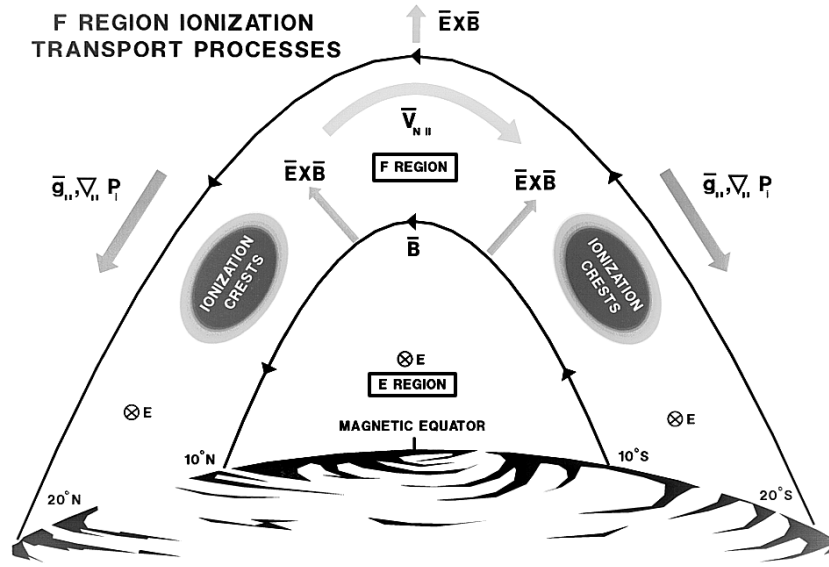


Figure 2.2: Appleton Anomaly formation after *de La Beaujardiere et al.* [2004]. The Equatorial Fountain is indicated by the upward $\mathbf{E} \times \mathbf{B}$ drift arrow at the top of the figure. Note the \mathbf{E} field has been mapped from the E-region to the F-region along the magnetic field lines which act as equipotentials. Plasma is then driven down the field lines by gravity $\mathbf{g}_{||}$ and pressure gradient $\nabla_{||}\mathbf{P}_1$ forces. The meridional neutral wind, $\mathbf{V}_{n||}$ is also shown.



Figure 2.3: Rayleigh Taylor Instability image from <http://web.arizona.edu/fluid-lab/rayleigh.html>. A dense fluid is held aloft by a less dense fluid below. A perturbation can trigger overturning, leading to the production of lower density structures (bubbles) that rise through the denser fluid. In this figure, the dense fluid is white.

inflection point of the sinusoidal discontinuity since the current is larger ($\propto n$) in the dense region. In response to the charge accumulation, polarization E fields develop as shown. Subsequent $\mathbf{E} \times \mathbf{B}$ drift causes the less dense plasma to rise and the dense plasma to sink, amplifying the perturbation and eventually leading to overturning and bubble formation.

Using linear perturbation theory and assuming a sinusoidal perturbation as above, a simple expression for the growth rate γ_{RT} of the EPBs is found to be:

$$\gamma_{RT} = \left(\frac{\mathbf{g}}{\nu_{in}} \right) \frac{1}{n_0} \frac{\partial n_0}{\partial z} \quad (2.10)$$

A derivation can be found in *Kelley* [1989, chap: 4]. Gravity, \mathbf{g} and density gradient, $\frac{\partial n_0}{\partial z}$, were introduced in our discussion of Figure 2.4, although here we are no longer considering a simple step-function. For fastest growth, the plasma gradient $\frac{\partial n_0}{\partial z}$ should be positive (dense fluid aloft) and large. The ion-neutral collision frequency, ν_{in} , enters through the Pederson conductivity (*Kelley* [1989, see]) and should be

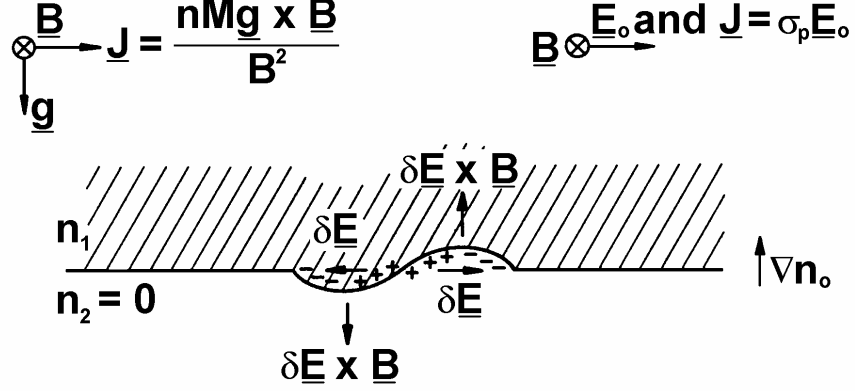


Figure 2.4: Perturbation Growth [*Kelley, 1989*]

small, as it is at high altitudes. Recall the pre-reversal enhancement drives the F-layer upwards near sunset, further decreasing ν_{in} . Equation (2.10) accounts for the role played by the gradient and ion-neutral collision frequency, but other forcing mechanisms can drive the instability, including an eastward electric field E and the neutral wind u_n .

Beginning with the gravitationally driven drift current shown in Figure 2.4, and adding terms for the eastward electric field and the neutral wind, we obtain:

$$J \approx \frac{n m_i g}{B} + \sigma_p \mathbf{E} + \sigma_p (\mathbf{u}_n \times \mathbf{B}) \quad (2.11)$$

Recalling

$$\begin{aligned} \sigma_p &= \frac{n m_i \nu_{in}}{B^2} \text{ and substituting} \\ J &\approx \frac{n m_i g}{B} + n m_i \frac{\nu_{in} E}{B^2} + n m_i \nu_{in} \frac{u_n B}{B^2} \end{aligned} \quad (2.12)$$

when the ratio of cyclotron frequency to species–neutral collision frequency, κ for ions $\kappa_i \gg 1$ and $\kappa_e \gg \kappa_i$. Further simplifying,

$$J \approx g + \frac{\nu_{in} E}{B} + \frac{\nu_{in} u_n B}{B} \quad (2.13)$$

$$J \approx \frac{g}{\nu_{in}} + \frac{E}{B} + \frac{u_n B}{B} \quad (2.14)$$

Thus the first term of (2.14) is in a form equivalent to the gravitational term in Equation (2.10). We can now append the corresponding electric field and neutral wind terms to Equation (2.10):

$$\gamma_{RT} = \frac{g}{\nu_{in}} \frac{1}{n_0} \frac{\partial n_0}{\partial z} + \frac{E}{B} \frac{1}{n_0} \frac{\partial n_0}{\partial z} + u_n \frac{1}{n_0} \frac{\partial n_0}{\partial z} \quad (2.15)$$

$$\gamma_{RT} = \frac{1}{n_0} \frac{\partial n_0}{\partial z} \left(\frac{g}{\nu_{in}} + \frac{E_0}{B} + u_n \right) \quad (2.16)$$

An eastward (positive) electric field and a downward (positive) neutral wind contribute to growth, however there is typically no strong downward neutral wind component. The neutral wind still plays a role, however, if the plasma layer is tilted with respect to the vertical. This can happen locally in response to the pre-reversal enhancement. The addition of a horizontal component of ∇n allows the eastward neutral wind to influence the stability. Letting σ refer to the angle the gradient ∇n makes with the horizontal and accounting for the eastward and upward components of the electric field, we obtain:

$$\gamma_{RT} = \frac{1}{n_0} \frac{\partial n_0}{\partial z} \left(\frac{g}{\nu_{in}} \cos \sigma + \frac{E_0^{east}}{B} \cos \sigma + \frac{(E_0^{up} + u_n^{east} B)}{B} \sin \sigma \right) \quad (2.17)$$

Earlier in this section we said the bubble growth occurs as the Earth rotates into darkness. During the day, the E–region dynamo overwhelms the F–region dynamo, inhibiting bubble growth. During the night, however, the E–region decays, the F–region dynamo dominates, and bubbles can grow. To capture this diurnal behavior, we include the weighted average of the field–line integrated Pederson conductivities

Σ_p in the E and F region:

$$\gamma_{RT} = \frac{\Sigma_P^F}{\Sigma_P^F + \Sigma_P^E} \frac{1}{n_0} \frac{\partial n_0}{\partial z} \left(\frac{g}{\nu_{in}} \cos \sigma + \frac{E_0^{east}}{B} \cos \sigma + \frac{(E_0^{up} + u_n^{east} B)}{B} \sin \sigma \right) \quad (2.18)$$

Equation 2.18 now captures the diurnal behavior of plasma bubble formation and accounts for the influence of the density gradient $\frac{1}{n_0} \frac{\partial n_0}{\partial z}$ which should be strong and directed upward, the eastward electric field and eastward neutral wind.

EPBs have been the subject of research for decades, although they were mysterious phenomena on remote sensing imagery before the cause was determined. At first, the term Equatorial Spread-F (ESF) was used to describe the ionosonde returns observed when EPBs were encountered. The reflected echo depicted a spread-F region, either in frequency or range. In the 1970s, returns from a 50 MHz radar at Jicamarca, Peru displayed structures referred to as plumes. In the subsequent decades, the cause of the unusual returns was identified as EPBs. Much of what has been learned about EPBs is summarized by *Schunk and Nagy* [2000] and more recently by *Dandekar and Groves* [2004] and *de La Beaujardiere et al.* [2004]. Table 2.2.2 presents a synopsis. The number of EPBs parallels the solar cycle and peaks at the equinoxes, but shows little response to day to day variations in solar flux or geomagnetic activity. Seasonal activity is linked to the Equinoxes for GPS frequencies, but at VHF wavelengths peak activity differs by longitudinal sector. Individual bubbles begin to form about an hour after sunset and each lasts for about 80 min. The bubbles tend to form every 160 min, with peak activity around 2200L. Two to three bubbles form each day. The longitudinal extent of the activity spans 1000s of kilometers. The bubbles drift eastward anywhere from 100-200 m/s [*Immel et al.*, 2003], tilting westward with height. Their vertical velocity typically ranges from 100-500 m/s although velocities can be ten times faster. They tend to form fossil-bubbles (no longer actively growing) as the night wears on and upward drift subsides. The plasma density can drop as much as 10^2 from the outside to the inside of an EPB, and this density variation is critical to scintillation.

Table 2.2: Temporal and Spatial Characteristics of Equatorial Plasma Bubbles & Scintillation based on remote sensing and in-situ data, compiled from *Schunk and Nagy* [2000], *Dandekar and Groves* [2004], *Immel et al.* [2003], and K. Groves (personal communication, 2006).

Temporal Characteristics	
solar/seasonal sensitivity	parallels solar cycle but no short term $\langle F10.7 \rangle$ solar flux dependence; worst at Equinox,
geomagnetic sensitivity	worst under Appleton Anomaly crests, less at geomagnetic equator. No correlation with K_p or D_{st}
individual bubble duration	1:20h
interval between formation	2:40h
# bubbles d^{-1}	2-3
daily cycle	begins $\approx 1h$ after sunset, peaks 2200L, dissipates by sunrise
Spatial Characteristics	
longitudinal extent of activity	1000s km
longitudinal EPB interval	10–1000 km
horizontal velocity	100–200m/s
vertical velocity	100–500 m/s, 40% reach 500–5000 m/s
vertical extent	≈ 100 –1500 km
trajectory	drift eastward, tilt westward with height
decay	”fossil” bubbles form as Spread- F & upward drift ends
density variation	up to 10^2 lower plasma density inside EPB

2.3 Scintillation: A Consequence of Ionospheric Irregularities

The final step toward understanding scintillation effects on GPS culminates with a discussion of scintillation itself. We will define scintillation and examine its influence on EM waves. The section will conclude with a discussion of research, measurement and modeling. First, however, we must understand how EM waves travel through a plasma.

2.3.1 Wave Propagation in Plasma. For simplicity, consider the dispersion relation for EM waves propagating in a cold, unmagnetized, isotropic electron plasma given by:

$$\omega^2 = \omega_p^2 + c^2 k^2 \quad (2.19)$$

$$\text{where } \omega_p^2 \equiv \frac{4\pi n_e e^2}{m_e} \quad (2.20)$$

The terms are the frequency of the transmitted wave, ω , the plasma frequency, ω_p , the wave number, k , and the number density of electrons, n_e . The phase velocity can be extracted by rearranging the terms:

$$v_p^2 \equiv \frac{\omega^2}{k^2} = \frac{\omega_p^2}{k^2} + c^2 > c^2 \quad (2.21)$$

Similarly, the group velocity is given by:

$$v^2 g \equiv \frac{d\omega}{dk_r} = c \left(1 - \frac{\omega_p^2}{\omega^2} \right)^{\frac{1}{2}} \frac{k_r}{k} < c \quad (2.22)$$

where k_r is introduced representing the real portion of the wave number. As an EM wave passes through a plasma, the phase velocity is advanced, and the group velocity delayed. This results in overestimated GPS code pseudoranges and underestimated carrier pseudoranges. Further manipulations involving the refractive index produce

the following relationships:

$$\Delta_{ph}^{Iono} = \frac{-40.3}{f^2} \int n_e d_{s0} \quad \Delta_{gr}^{Iono} = \frac{40.3}{f^2} \int n_e d_{s0} \quad (2.23)$$

where Δ represents the difference between measured and geometric range, the constant 40.3 arises from a Taylor series expansion of the phase refractive index, and integration occurs along the geometric path d_{s0} [Hofmann-Wellenhof *et al.*, 2001]. The quantity $\int n_e d_{s0}$ is the Total Electron Content (TEC). The important point from Equation (2.23) is that using the relationship between TEC and frequency, the ionospheric refraction can be exploited to obtain TEC measurements from dual frequency receivers and conversely, the same relationship can be modeled to remove the ionospheric refraction from single channel receivers as described by Klobuchar [Parkinson *et al.*, 1996].

2.3.2 Definition, Characteristics and Models. The situation for scintillation, sadly, is not so simple. Groves *et al.* [1996] provide a concise description of scintillation:

Scintillation of radio waves occurs when the waves encounter small-scale spatial variations in refractive index. . . Because the scattering and refractive properties of the medium vary along an incident wave front, the transmitted wave front is composed of a mixture of varying amplitude and phase and an irregular interference pattern results. . . The scintillation observed on the ground is an indication of the rate at which the interference pattern drifts past the observer, determined by the physical drift speed of the [EPBs], the velocity at which the source wave is cutting across the ionosphere due to satellite motion, and the motion of the observer, if any.

To understand the relationship between refractive index \mathcal{N} and plasma density n , we return to the dispersion relation, Equation 2.19:

$$\omega^2 = \omega_p^2 + c^2 k^2$$

The refractive index is defined as :

$$\mathcal{N}^2 = \frac{c^2}{(\omega/k)^2} \quad (2.24)$$

Substituting 2.24 into 2.19, we obtain:

$$\mathcal{N}^2 = 1 - \frac{\omega_p^2}{\omega^2} \quad (2.25)$$

Recalling Equation 2.20 and substituting in 2.25:

$$\mathcal{N}^2 = \left(1 - \frac{4\pi n_e e^2}{m\omega^2}\right) \quad (2.26)$$

Differentiating with respect to x and rearranging terms:

$$\frac{d\mathcal{N}}{dx} = \left(-4\pi e^2 \frac{dn_e}{dx}\right) / \left(m\omega^2 \left(1 - \frac{4\pi n_e e^2}{m\omega^2}\right)^{1/2}\right) \quad (2.27)$$

This shows that the change in refractive index over a distance is directly proportional to the change in electron density over that same distance. Recall from Table 2.2.2 that the plasma density can change by two orders of magnitude across an EPB. Figure 2.5 is an artistic interpretation of the interference pattern caused by the EPBs. As EM waves pass through ionospheric density depletions, the waves are refracted and scattered, leading to “patches” of focused and defocused energy. The arrow shows these “patches” drifting past the receiver (person) located on the ground. The final result is fluctuations in the intensity of the received signal

Researchers have historically modeled scintillation using a one-dimensional phase screen. A 1-D phase screen can be thought of as an arrangement of lenses alternately focusing or defocusing the incident EM energy as it passes through the screen. The screen moves relative to the transmitter and receiver as described above. A simple model of a discrete phase screen is described by *Knight* [2000] depicted in Figure 2.6:

In the figure, the shaded circles labeled I represent “rod like lenses aligned to the Earth’s magnetic field”, dx describes a portion of the phase screen and r is the distance to the elements [*Knight*, 2000, Appendix A]. He gives the complex amplitude

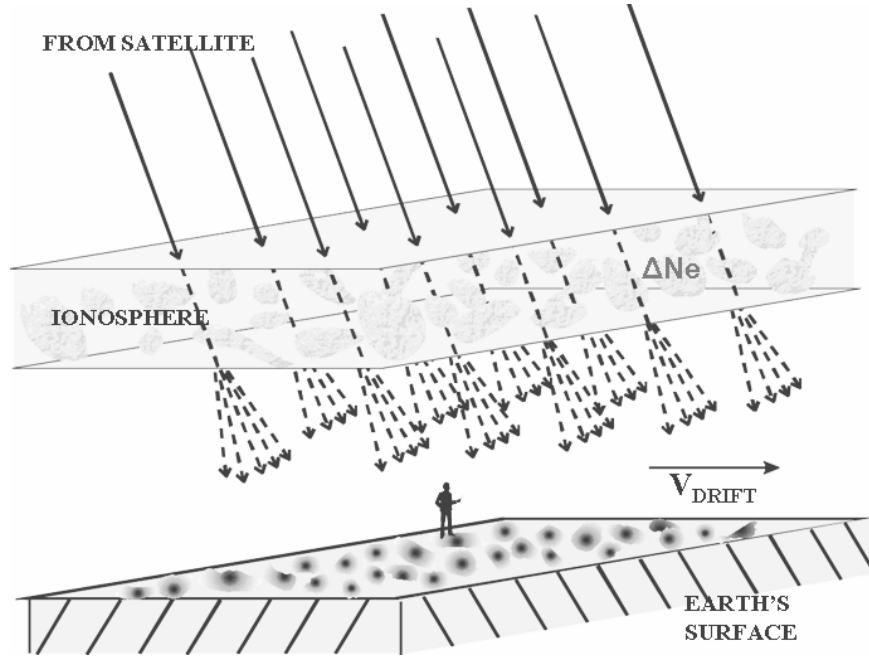


Figure 2.5: Illustration of scintillation. As EM waves pass through ionospheric density depletions, the waves are refracted and scattered, leading to “patches” of focused and defocused energy. The arrow shows these “patches” drifting past the receiver (person) located on the ground. The final result is fluctuations in the intensity of the received signal.

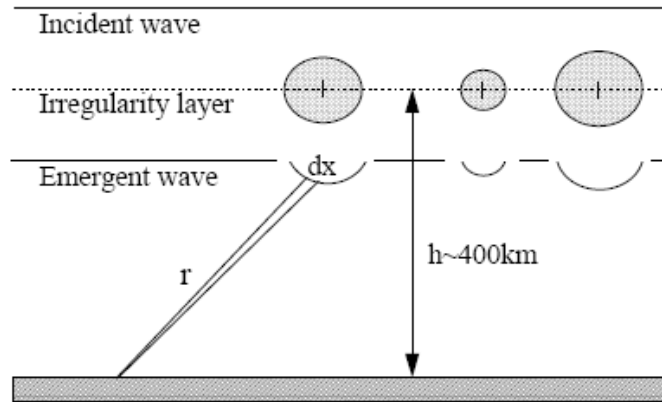


Figure 2.6: Illustration of a thin Phase-Screen model of scintillation by *Knight* [2000] the shaded circles labeled I represent “rod like lenses aligned to the Earth’s magnetic field”, dx describes a portion of the phase screen and r is the distance to the elements.

of the signal as:

$$I = \frac{1}{\sqrt{r\lambda}} \left(1 - 2 \int_{ir} \sin(P_0 + \Phi/2) \sin \Phi/2 \, dx \right) \quad (2.28)$$

$$Q = \frac{1}{\sqrt{r\lambda}} \left(2 \int_{ir} \cos(P_0 + \Phi/2) \sin \Phi/2 \, dx \right) \quad (2.29)$$

where I and Q represent the in-phase and quadrature components of the signal, Φ is the phase perturbation produced by the lenses, and $P_0 = -\pi/4 - 2\pi(r - h)/\lambda$, and the quantity $\sqrt{r\lambda}$ is the Fresnel radius, z_f . The Fresnel radius indicates whether an ionospheric irregularity will have an impact on amplitude. If the scale of the irregularity is much larger, amplitude variations are minimal. At or below z_f , amplitude variations are significant. Variations are also significant if strong density gradients are present [Knight, 2000, Appendix A.]. Beach *et al.* [2002] studied the phase screen model and found it generally able to produce an estimate of the magnitude of amplitude scintillation within 90% of its true value when “only a few (≈ 5) evenly spaced samples per Fresnel radius” are obtained. z_f for GPS frequencies is ≈ 300 -400 m. The severity of amplitude scintillation is expressed in terms of the S_4 index, where

$$S_4 = \frac{\sqrt{\langle I^2 \rangle - \langle I \rangle^2}}{\langle I \rangle}. \quad (2.30)$$

In Equation (2.30) I is the signal intensity measured at the receiver [Fremouw *et al.*, 1980], or the square of the amplitude. Equation 2.30 is simply the signal intensity standard deviation divided by its mean, with sampling rates and averaging periods appropriate for the signal being characterized, and is valid for weak to moderate levels of scintillation. Davies [1990] presents a model of the S_4 index based on physical parameters:

$$S_4 = B \lambda^3 Z L K \sec^2 \chi \langle \Delta n_e^2 \rangle \quad (2.31)$$

where B is a parameter that depends on “geometrical factors, fundamental constants, etc”, λ is the wavelength of the carrier, Z and L are the layer thickness and height,

respectively, χ is the angle between the vertical and the ray, and $\langle \Delta n_e^2 \rangle$ is the mean square deviation of the electron number density. As well as directly linking S_4 to electron number density, this equation shows S_4 increasing as the path nears the horizon.

Thus far, we have linked EPB-induced plasma density variations to amplitude fluctuations that can be characterized by the S_4 index. This development can be taken a step further by relating the S_4 index to the amount of signal fade at the receiver. This is accomplished through the Nakagami-m probability density function:

$$P(A) dA = dA \frac{2m^m A^{2m-1}}{\Gamma(m) \langle A^2 \rangle^m} \exp \left(-m \frac{A^2}{\langle A^2 \rangle} \right) \quad (2.32)$$

where Γ is the gamma-function, A is the amplitude, and

$$m = 1/S_4 \quad (2.33)$$

Wheelon [2003, chap. 10] points out that “ $m = 1$ corresponds to a Rayleigh distribution and $m = 1/2$ corresponds to a one-sided Gaussian distribution.” He notes the fit of S_4 and signal fade to the Nakagami-m distribution is empirical and not derived from first principles. Figure 2.7 depicts the Nakagami-m PDF where “The curves are each normalized so that the maximum likelihood corresponds to unit probability” [*Wheelon*, 2003]. The take-away is as m becomes smaller (and hence S_4 becomes larger) the range of likely amplitude values *increases*. Finally, *Knight* [2000] notes the S_4 index scales as $S_4 \propto f^{(-p+3)/4}$ where f is the carrier frequency, p is the spectral index (typically 2.5 at equatorial latitudes), when $S_4 < 0.5$ (weak to moderate scintillation). By the scaling equation, the GPS L2 frequency (which is lower) will be more susceptible to scintillation than the L1 frequency, by a factor of 1.4 according to *Knight* [2000]. This has implications for dual frequency GPS users: if scintillation is strong enough to cause outages on L1, L2 will probably be unavailable as well.

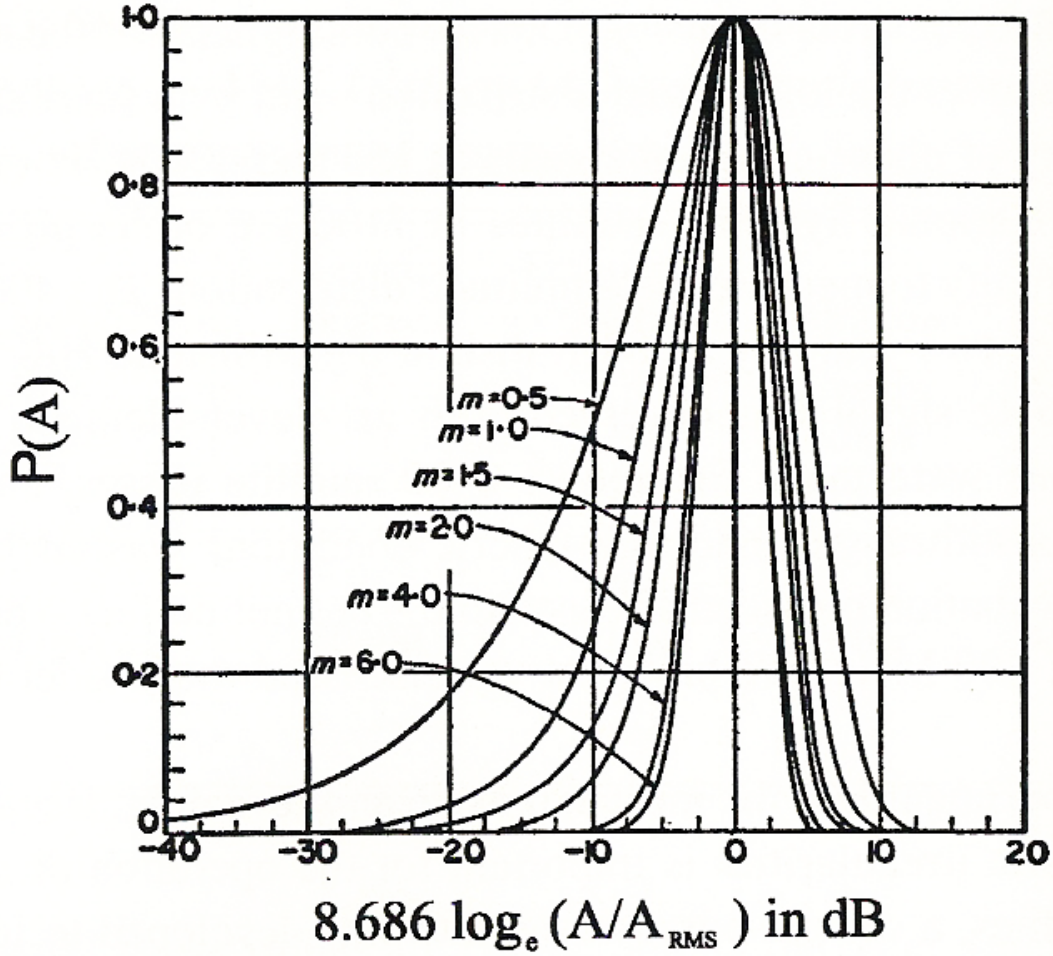


Figure 2.7: Nakagaim-m Probability Density Function by *Wheelon* [2003]. A is amplitude and A_{RMS} is the root-mean-square amplitude. “The curves are each normalized so that the maximum likelihood corresponds to unit probability” [Wheelon, 2003]. Notice as m becomes smaller (and hence S_4 becomes larger) the range of likely amplitude values *increases*.

Thus far, we have reviewed the characteristics of GPS and the ionosphere. Within the ionosphere, we have examined the development of EPBs and their role in scintillation. We have seen how the changes in refractive index arising from plasma density gradients within the EPBs alter EM waves passing through them, and thus alter the GPS signals. We saw that the amplitude fluctuations caused by scintillation can be characterized by the S_4 index. Finally, we were able to relate the S_4 values to levels of signal fade at a receiver through the Nakagami-m probability density function. The last portion of Chapter II will be devoted to a review of some of the literature published about scintillation and GPS.

2.3.3 Research on Scintillation and its Impacts on GPS. Literature on scintillation and GPS can be divided into observational and modeling studies and comparisons of the two. In the past decade, a network of GPS receivers to monitor scintillation, as an enhancement to the Scintillation Decision Aid (SCINDA) [Groves *et al.*, 1997], was deployed throughout the equatorial ionosphere. Consequently, large data sets have become available for analysis. Additionally, in-situ measurements of plasma irregularities have continued and will expand with the anticipated launch of the Communication/Navigation Outage Forecasting System (C/NOFS) [de La Beaujardiere *et al.*, 2004].

Groves *et al.* [1996] presented some findings regarding scintillation and L-band satellites through 1996. Early data from GPS receivers indicated signal fades exceeding 15 dB were possible and more than one GPS satellite could potentially be dropped during a scintillation event. His follow-up 1997 paper [Groves *et al.*, 1997] described the SCINDA network and the temporal and spatial variations of L-band scintillation in the Atlantic and Americas sector, along the magnetic dip equator as well as under the anomaly crest. This information has already been presented in Table 2.2.2 and will not be repeated here.

By 2001, the SCINDA network had grown and with it, the knowledge of scintillation impacts on GPS. Additionally, the solar cycle had reached its peak, providing

additional fodder for comparisons. *Thomas et al.* [2001] presented findings from the Pacific sector. In addition to annual summary plots of scintillation levels at Marak Parak and Parepare showing the seasonal and diurnal peaks, he presented regional correlation data that showed if any satellite in the region experienced $S_4 > 0.6$ on at least one link during the night, “there was a mean probability of 75% that the other stations in the network will have at least one link which also records scintillation above $S_4 = 0.6$ on that night”. He also presented the number of satellite links surviving during scintillation episodes, finding that up to 40% of the links were affected under moderate scintillation ($S_4 > 0.6$), and over 90% for weak scintillation ($S_4 > 0.3$), markedly higher than earlier estimates. In his estimation, this not severe enough to significantly hamper navigation because the episodes were short lived.

Datta-Barua et al. [2003] compared the scintillation impacts on single and dual-frequency GPS users. They found both susceptible to impacts from equatorial scintillation, with the L2 frequency more prone to interruptions. They also note if L2 is lost, dual frequency users can substitute the ionospheric model available to single frequency users and essentially obtain the same precision and availability as L1 users. *Thomas et al.* [2004] studied GPS precision degradation in the Pacific sector caused by scintillation during the 1998-2002 portion of the solar cycle. Errors up to 30 m were discovered, with an “underlying seasonal modulation from about 5 m to 15 m”.

At the same time SCINDA was gaining momentum, serious efforts at modelling ionospheric scintillation produced the WideBand MODel (WBMOD) in 1995. WBMOD is based on climatology and the one-degree phase screen model [*Rino*, 1979b]¹. Naturally, comparisons between predicted and observed conditions began. In 1999, *Knight et al.* [1999] compared predictions with observations in the Pacific sector. They found good agreement between modeled and predicted observations. A similar study by *Cervera et al.* [2001] supported the earlier work for periods of low sunspot activity, except WBMOD ended scintillation prematurely at night. They

¹A description of this current model can be found at <http://www.nwra-az.com/ionoscint/wbmod.html>.

found WBMOD performed poorly during solar maximum at the equatorial stations, underestimating scintillation in some cases by an order of magnitude. WBMOD also predicted the end of nightly scintillation two hours earlier than was observed. Since many weapons systems rely on GPS, a logical step was to investigate the impact of scintillation on various weapons systems. In a modeling study of B-1B and F-15E weapons platforms, *Evans* [2005] demonstrated that scintillation degrades accuracy and can, if occurring in conjunction with jamming, render GPS unavailable.

In the intervening years since *Thomas et al.* [2001], more has been learned about scintillation and GPS. Thomas’ original exploration and particular presentation, however, was never expanded to include other sites or years. *Thomas et al.* [2001] wrote “It is desirable to have a more rigorous statistical analysis of the S_4 database for specific S_4 thresholds, for example, as a function of local solar time and day or month of the year.” Our work takes up this challenge for additional years and longitudinal sectors. Additionally, we’ll examine the influence of imputation on the resulting climatology, and take the analysis a step further by calculating HDOP based on the sequential removal of satellites experiencing given levels of scintillation. The remaining chapters are devoted to this analysis.

III. Method

CREATING and analyzing statistics first requires data. We begin this chapter by describing the source and characteristics of the data we used. Data must also be scrutinized to remove undesirable artifacts. We outline the preparation of the data and discuss the events surrounding missing data. Finally, we detail the processing of the data.

3.1 Data Description

We examined SCINDA data provided by the Air Force Research Laboratory (AFRL). Keith Groves (2006, personal communication) suggested beginning our analysis with data from Ascension during the last solar maximum (2001). Its position under the Appleton Anomaly crest should provide a rich scintillation environment. The Pacific sector station used for comparison was Parepare during 2000, also under the anomaly crest. We also analyzed data from Ancon, which lies close to the magnetic dip equator and a corresponding Pacific sector station, Marak Parak, both from 2001. Data from the off solar peak years 1999 and 2002 at Ancon, Ascension, Marak Parak, and Parepare, as well as 1998 at Marak Parak and Parepare, and 2003 at Ancon and Ascension were also examined. Characteristics are shown in Table 3.1. Site locations are shown in Figure 3.1 (a) and (b).

Table 3.1: SCINDA Site Characteristics. Negative signs indicate South Latitude or West Longitude. Magnetic data from International Geomagnetic Reference Field (IGRF10) and are approximately centered on the data period.

Location	ID	Lat °	Lon °	Years	Elev m	Dip \angle °
<i>Ancon</i>	GB	-11.78	-77.15	98-04	53	1.57
<i>Ascension</i>	GE	-7.94	-14.39	99-04	160	-39.87
<i>Marak Parak</i>	GV	6.31	117.40	97-02	34	-3.13
<i>Parepare</i>	GW	-3.98	119.65	97-03	65	-25.63

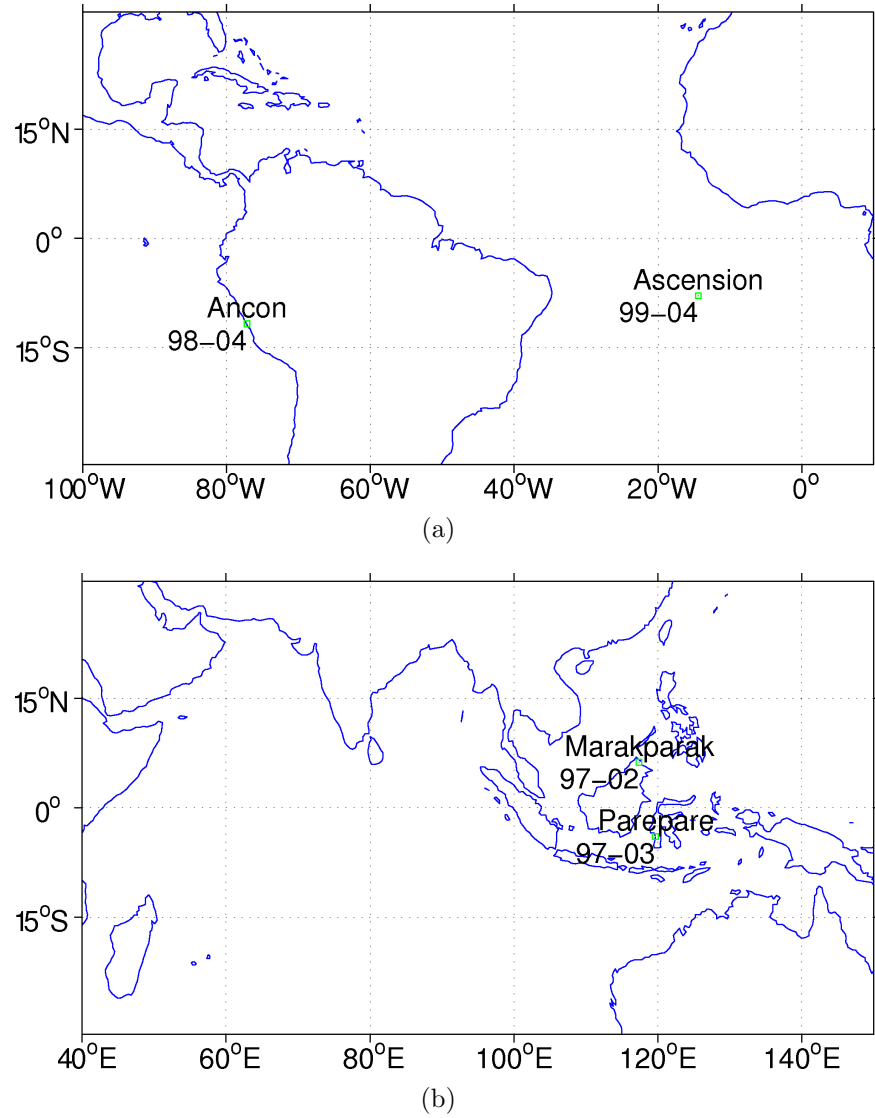


Figure 3.1: Scintillation Network Decision Aid (SCINDA) sites in the (a) Atlantic & Americas and (b) Pacific sectors used in this research. The operational years are included in the lower left quadrant of each location

Two types of GPS receivers were used to collect data at these locations, a NovAtel 11-channel narrow correlator receiver described by *Dierendonck et al.* [1996] or an Ashtech ZY-12 described by *Milner* [2002]. Signals were sampled at 50 Hz and 20 Hz respectively and recorded each minute. An example of the raw data record is contained in an appendix. The following data were recorded:

- Receiver Latitude and Longitude (Decimal °)
- Year
- Day of Year
- Time (s)
- PRN
- S_4
- SV elevation & Azimuth (Decimal °)
- SV Latitude & Longitude (Decimal °)
- Assumed 300 km Ionospheric Pierce Point Latitude & Longitude

3.2 Data Preparation and Irregularities

FORTTRAN code written by C. Leakeas (personal communication, 2006) was used to reformat the data from its original tabular form to a columnar form more amenable to `Matlab`[®] ingest. During reformatting, all records from satellites below 15° were excluded as a first attempt at mitigating the effects of multipath¹. The remaining observations presented two irregularities. The first, and easiest to reconcile, was an S_4 value of 9.00 that appeared periodically. This was identified as “bad data” in the original record. According to Ron Caton (personal communication, 2007) 9.00 was ascribed during extreme levels of scintillation. Under extreme scintillation, early receivers would produce nonphysical S_4 values and these were replaced with 9.00.

¹see Subsection 2.1.3

When the elevation of the particular satellite was less than zero, S_4 of 9.00 was ascribed. This happened when incorrect ephemeris data was linked to the S_4 data months *after* the S_4 data had been collected. Since we applied a 15° mask in an effort to remove multipath, the remaining high values could be attributed to high levels of scintillation. Typically, high S_4 values surrounded the occurrence of 9.00, again supporting this conclusion. The receivers also recorded $1 \leq S_4 \leq 9.00$ during extreme levels of scintillation. During particularly bad scintillation conditions, drop-outs would occur and a particular satellite's S_4 value would not be recorded. This missing data presented another challenge that until now had not been addressed.

Data gaps occurred on time scales from minutes to months. It could affect as few as one to as many as all available satellites reporting in a given minute. Before attempting to understand the data that were present, it was necessary to study the circumstances surrounding the data that were absent. We originally limited our analysis to a time scale of minutes and to those missing records *bounded by* complete records. We began by determining how much data were missing.

In the introduction to his text on analyzing missing data, *Schafer* [1997] says “When the incomplete cases comprise only a small fraction of all cases (say, five percent or less) then case deletion may be a perfectly reasonable solution to the missing-data problem.” This assumes the data are missing at random. Examining 2001 data for Ancon, Ascension, and Marak Parak, the fraction of bounded data missing was three percent or less for all but Ascension, which was approximately eight percent. Ignoring the data seemed plausible at three of four sites. However, a significant fraction of the missing data might be associated with strong scintillation, in other words, Missing Not At Random (MNAR)². Ignoring the those data could underestimate scintillation impacts.

²For definitions of missing data mechanisms, and a good introduction to dealing with missing data, see James Carpenter and Mike Kenward's website at <http://www.lshtm.ac.uk/msu/missingdata/index.html>

We studied characteristics of the outages in 2000 and 2001 in an attempt to separate those related to scintillation from those related to other causes (e.g. multipath, equipment failure, etc.). Figure 3.2 shows the cumulative distribution of bounded data outages in 2001 for Ascension and Ancon. In all cases, 85% or more of the outages lasted 10 min or less. This suggests most outages are associated with brief interruptions associated with scintillation.

We also examined the relationship of outage duration to the day of year. Figure 3.3 shows this relationship for Ascension (a), Ancon (b), Parepare (c) and Marak Parak (d). The number of long-duration outages peaks at Ascension near the equinoxes, indicating a link to scintillation (recall Table 2.2.2). This behavior was less evident at the other stations. The longer duration outages exhibited some structure across days. They were particularly prominent at Parepare (c), but can also be seen at Marak Parak (d) and Ascension (a). We suspected satellites were skirting the 15° mask³ on these days, leading to long-term outages.

To confirm our suspicions, we examined a plot of elevation angle just prior to an outage versus outage duration for these stations. The results are shown in Figure 3.4. For the Pacific longitudinal stations at Parepare (c) and Marak Parak (d), the evidence is clear that the longer duration outages were associated with elevation angles below 20° . Additionally, the gentle rise in outage duration from high elevation angles to elevation angles just above 20° hints that scintillation susceptibility increases as the satellite nears the horizon. This is consistent with Equation 2.31 which showed S_4 increasing as the χ angle approached 90° . This is also intuitively satisfying since the possibility of multipath increases as the path nears the horizon. If multipath is excluded, the path-length through the ionosphere is greater at low elevations (high χ) and increases the probability of transiting a depleted region. Although the correlation for elevations less than 20° at Ascension (a) is less striking, the general trend of longer outages associated with lower elevation angles appears again.

³See Subsection 2.1.3

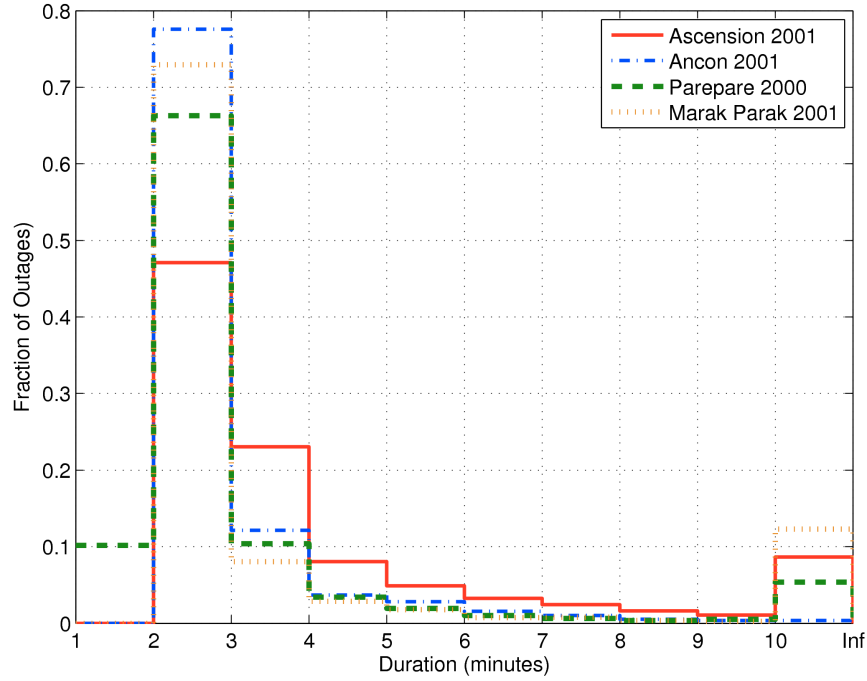


Figure 3.2: Distribution of Outage Durations at Parepare and Marak Parak in 2000, and Ascension and Ancon in 2001. Most outages ten minutes or less suggesting scintillation as the culprit.

Finally, Figure 3.5 is a plot of satellite elevation (black lines) and S_4 (blue lines) for a particular GPS satellite (PRN 28) for day 126 at Ascension in 2001 (Ron Caton, personal communication, 2007). The abscissa in this plot represents time centered on approximately 2200 UT, the ordinate on the left is S_4 level, on the right is elevation in degrees. Note the dotted line at the bottom of the figure represents the 10° elevation mask. In the center of the figure, in conjunction with the spike in S_4 values, note the elevation has slowly decreased to near the 10° mask. Since we were applying a 15° mask to our data, this would appear as an extended data gap.

Inspection of the distribution of outages for a given elevation angle before and after an outage and whether the satellite was ascending or descending produced the results shown in Figure 3.6. In the Atlantic & Americas sector at Ascension and Ancon, the link between low elevation angles and outages is readily apparent. The link is less obvious in the Pacific sector at Parepare and Marak Parak, but still present. Another interesting feature present at all sites but Ancon is a cluster of outages that

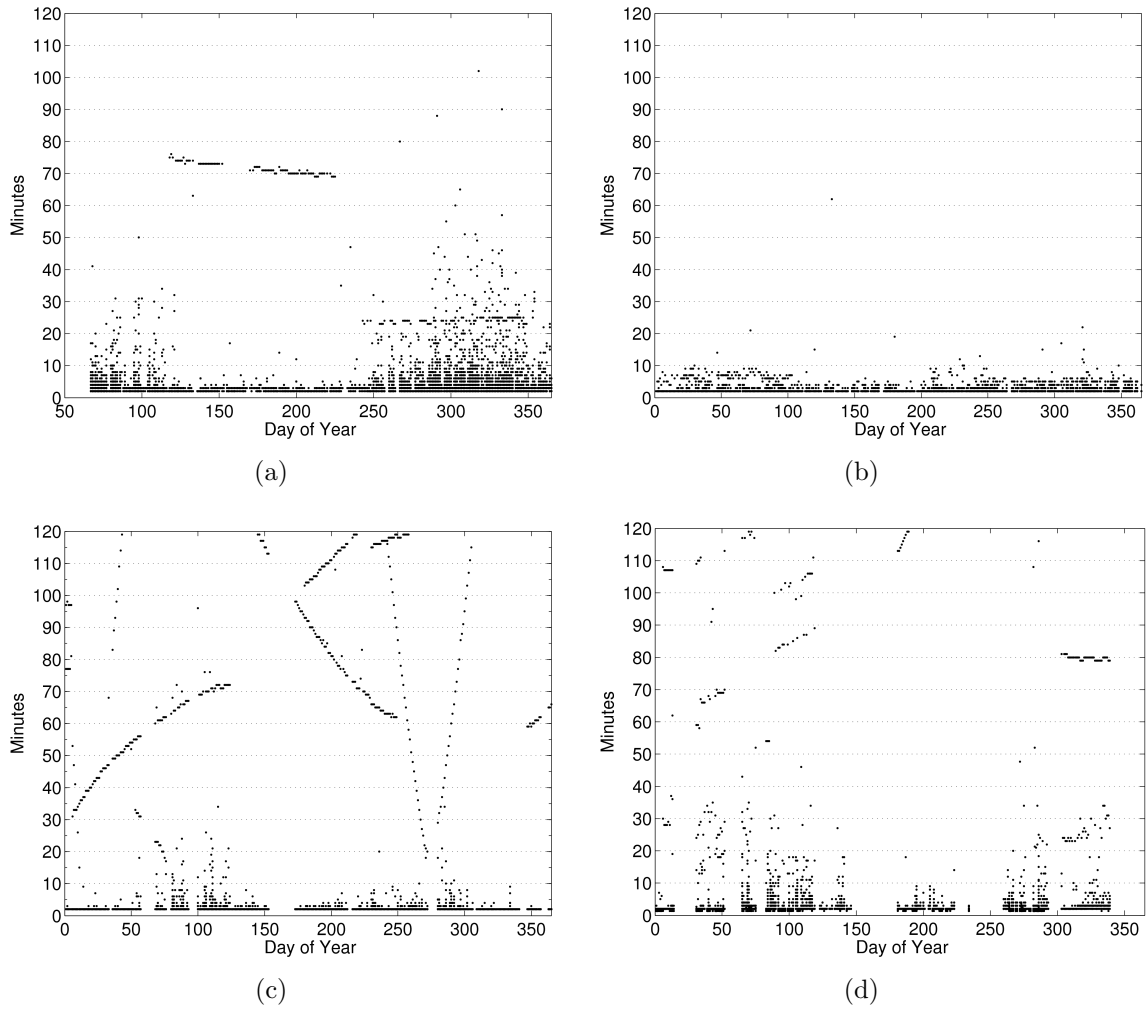


Figure 3.3: Day of year versus outage duration for Ascension (a) and Ancon (b) in 2001, and Parepare (c) and Marak Parak (d) in 2000 with a 15° elevation mask applied.

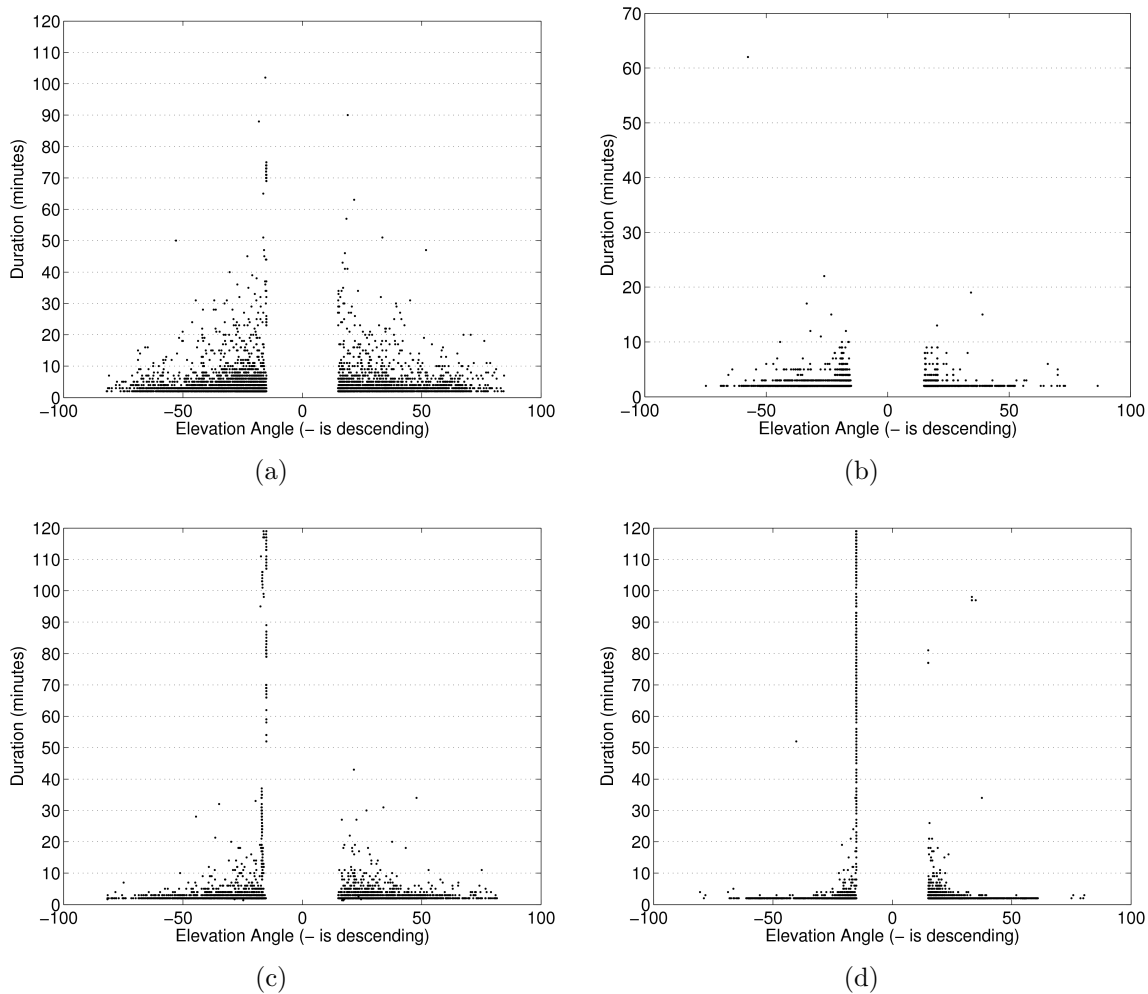


Figure 3.4: Elevation angle versus outage duration for Ascension (a) and Ancon (b) in 2001, and Parepare (c), and Marak Parak (d) during 2000 with 15° elevation mask applied.

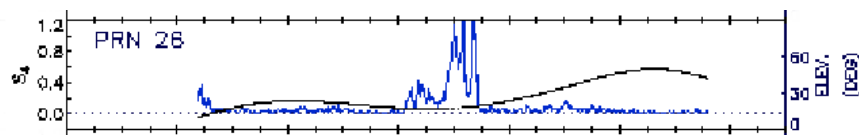


Figure 3.5: Satellite Elevation Near Mask. Plot of satellite elevation (black lines) and S_4 (blue lines) for a particular GPS satellite (PRN 28) for day 126 at Ascension in 2001. The abscissa in this plot represents time in half-hour increments centered on approximately 2200 UT, the ordinate on the left is S_4 level, on the right is elevation in degrees. Note the dotted line at the bottom of the figure represents the 10° elevation mask. (Ron Caton, personal communication, 2007)

began between 40° and 60° as the satellite is ascending. Comparison with outage duration in Figure 3.4 suggests these high elevation angle outages are short lived, and thus more likely to be associated with scintillation. The long-duration low elevation outages are more likely a consequence of satellite geometry (e.g. multipath, obstructions) and mask angle.

At this point we decided to examine the effect of excluding the outages below 20° elevation. By doing so, we were able to eliminate the structures associated with long duration outages, as seen in Figure 3.7. Although the structures had vanished, some long duration outages remained. We looked at outages lasting over 10 min at Marak Parak (Figure 3.7 (d)) in 2000 that persisted even after filtering the satellites below 20° . The characteristics of those outages are shown in Table 3.2. The first column of the table indicates the UTC day of year in which the outage occurred. The duration of the outage in seconds is shown in the second column. Columns 3–5 indicate the maximum S_4 before, during and after the outage as reported by the available GPS satellites. The final two columns indicate the elevation angle of the affected satellite immediately before and after the outage. The first five outages all occurred during benign scintillation conditions. Additionally, the outage durations are identical, the elevation angles are nearly so, and the outages occurred on five consecutive days. These facts point towards an outage mechanism other than scintillation. Of the remaining long duration outages in the Table 3.2, the one on day 50 also began during quiet scintillation conditions, with a high S_4 in the midst of the outage, followed by low S_4 at the end. The low S_4 values bordering the outage cast doubt on scintillation as the culprit, despite the anomalously high S_4 value during the outage. Outages on days 89, 110, 123 and 292 all began near the 20° threshold or ended near or below it, raising the specter of multipath or mask problems. Thus we are left with days 88 and 285 as potential scintillation candidates. These two days are near the equinox and so scintillation seems more likely, although the day 88 outage begins with a maximum reported S_4 of 0.2, again indicating quiescent conditions at onset. So of these 12 long

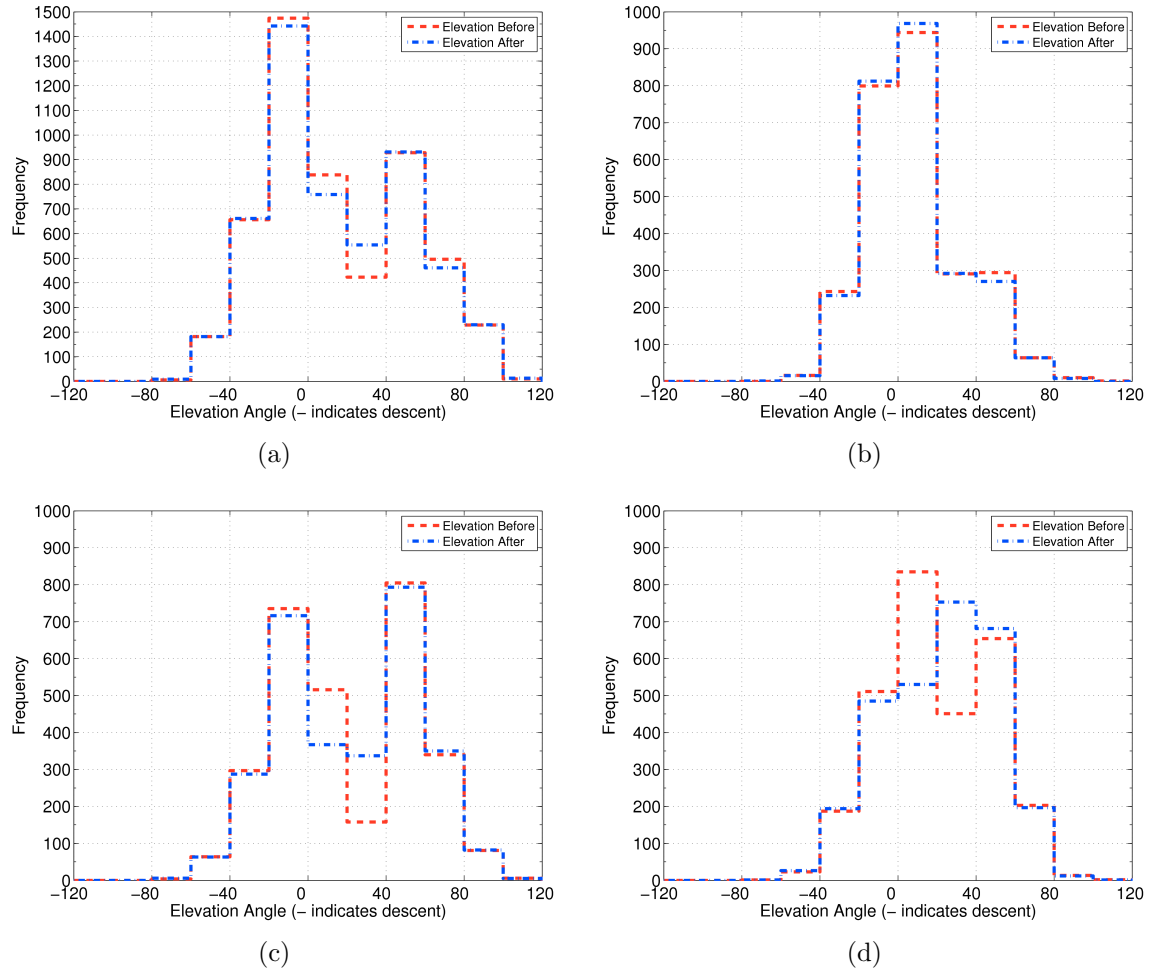


Figure 3.6: Elevation Angle Distribution Before and After Outage for Ascension (a) and Ancon (b) in 2001, and Parepare (c), and Marak Parak (d) during 2000 with 15° elevation mask applied. Negative values indicate descent.

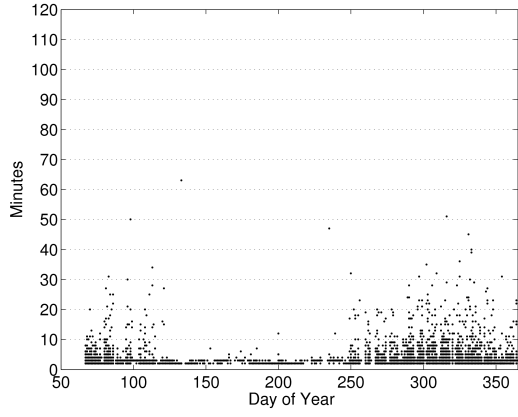
duration outages, 2 can be reasonably attributed to scintillation to the exclusion of other causes.

Finally, we looked at the correlation between $\sigma_{S_4}^2$ and $S_{4\ max}$. Figures 3.8 (a, c, e) show the correlation one minute before, during, and one minute after outages during 2001 at Ancon, while Figures 3.8 (b, d, f) show the same for Ascension. Table 3.3 contains the corresponding correlation coefficients. The high degree of correlation between the maximum S_4 and S_4 variance before and after the outages suggests that GPS constellation geometry and the scale of EPBs result in only a few satellites being scintillated at once. In other words, scintillation events typically affect one or two satellites during a given minute, leading to a large S_4 variance. The relationship between the maximum S_4 and S_4 variance described above may be useful to impute missing S_4 values within a given minute, i.e. choosing a replacement S_4 value such that the correlation between the maximum S_4 and $\sigma_{S_4}^2$ is maintained. Similar statistics have been used to distinguish between multipath and scintillation [Datta-Barua *et al.*, 2003].

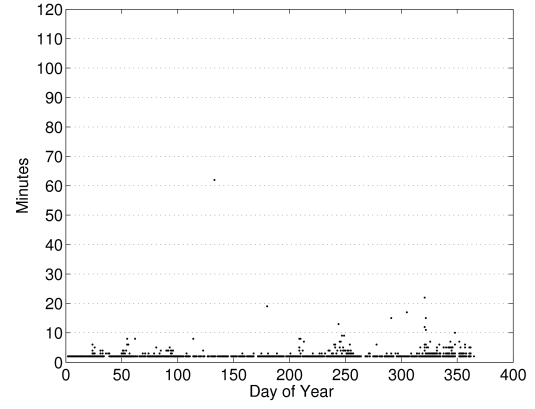
In addition to the single-satellite outages, outages involving *all* satellites occasionally occurred. Simultaneous outages accounted for up to approximately 34% of all outages as shown in Table 3.4 (a) at Parepare. However, S_4 was less than 0.3 in 85–90% of the simultaneous outages, as shown in Table 3.4 (b). Thus the majority of the simultaneous outages can be attributed to phenomena other than scintillation. Interestingly, however, the duration of simultaneous events was almost always two minutes or less.

Returning to the present research, although only four sites were sampled we are confident the following characteristics are applicable in general:

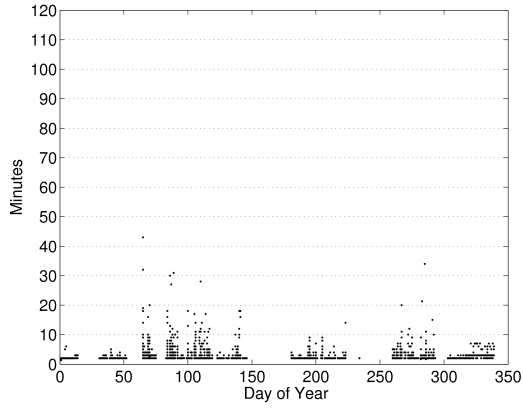
- Most outages are short, lasting less than ten minutes (Figure 3.2).
- Outages durations reflect to some degree the seasonal peaks in scintillation associated with the equinoxes, but also exhibit structures that are unrelated to scintillation (Figure 3.3).



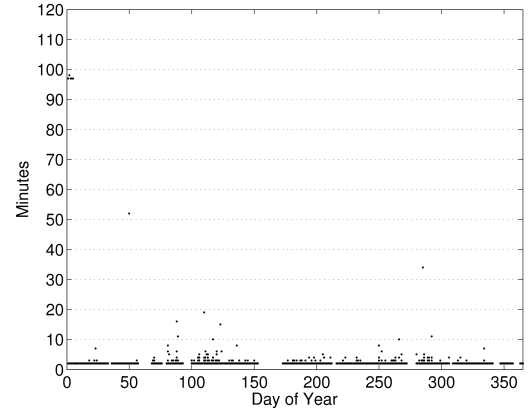
(a)



(b)



(c)



(d)

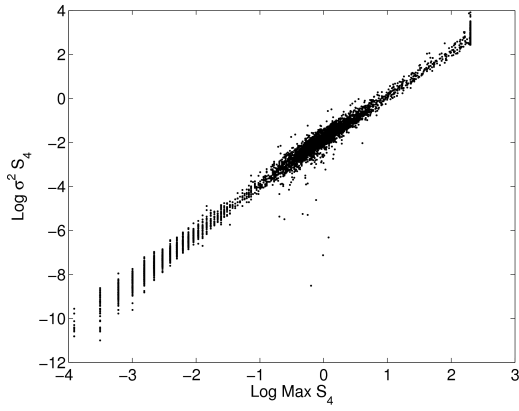
Figure 3.7: Day of year versus outage duration for Ascension (a) and Ancon (b) in 2001, and Parepare (c) and Marak Parak (d) in 2000 with a 15° elevation mask applied and outages below 20° excluded.

Table 3.2: Long Duration Outages at Marak Parak, 2000. The first column of the table indicates the UTC day of year in which the outage occurred. The duration of the outage in seconds is shown in the second column. Columns 3–5 indicate the maximum S_4 before, during and after the outage as reported by the available GPS satellites. The final two columns indicate the elevation angle of the affected satellite immediately before and after the outage.

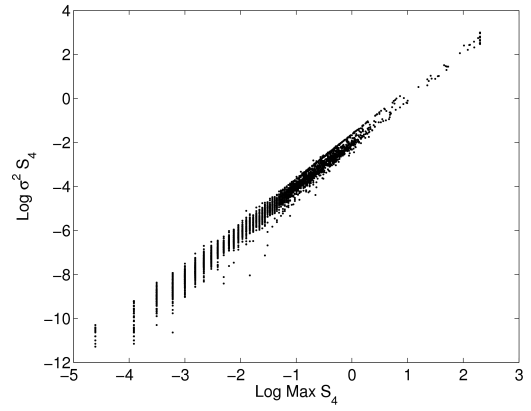
Day	Length	S_{4max}^{before}	S_{4max}^{during}	S_{4max}^{after}	Elev Before	Elev After
1	5820	0.06	0.11	0.04	34.97	34.63
2	5880	0.06	0.08	0.05	33.44	-34.22
3	5820	0.1	0.08	0.09	33.41	34.2
4	5820	0.14	0.28	0.08	33.39	34.18
5	5820	0.12	0.12	0.08	33.36	34.17
50	3120	0.04	5.83	0.06	-40.14	-18.25
88	960	1.1	0.34	9.00	23.6	29.27
89	660	0.74	0.2	0.94	20.05	23.68
110	1140	0.75	0.71	0.68	-21.05	-18.59
123	900	1.15	0.17	0.3	21.83	26.0
285	2040	0.2	0.99	3.7	37.54	45.05
292	660	1.06	0.31	0.75	-20.24	-18.08

Table 3.3: Correlation Coefficients for Max vs $\sigma^2 S_4$ showing the strong correlation between these parameters before and after an outage. The absence of the satellite during the outage degrades the correlation, as expected.

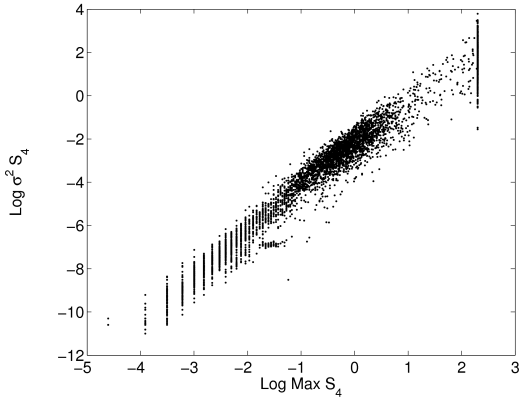
S_4 Max and σ^2 Outage Correlation Coefficients			
Site	Before Outage	During Outage	After Outage
Ancon	.94	.80	.96
Ascension	.95	.76	.95
Marak Parak	.95	.59	.95
Parepare	.94	.76	.95



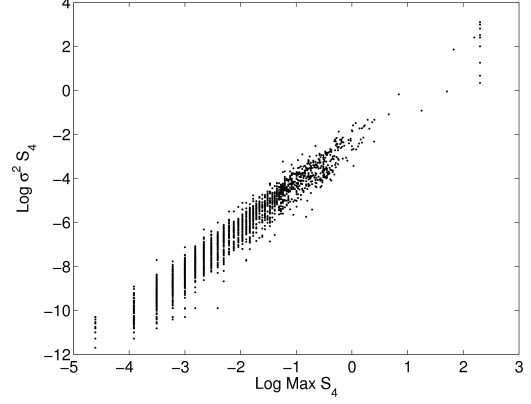
(a)



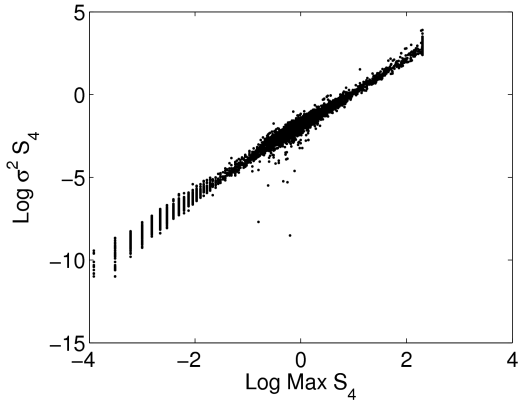
(b)



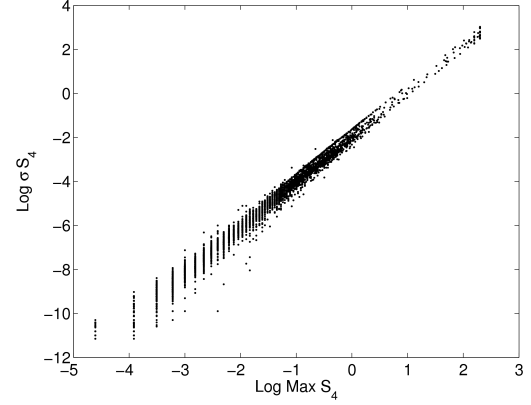
(c)



(d)



(e)



(f)

Figure 3.8: Relationship between maximum S_4 and $\sigma_{S_4}^2$ at Ascension (left column) and Ancon (right column) one minute before (a and b), during (c and d) and one minute after (e and f) each bounded outage in 2001. The correlation coefficients are given in Table 3.3. These figures seem to suggest the geometry of GPS satellites and the scale of EPBs leave a minority of satellites susceptible to scintillation, in most circumstances.

Table 3.4: Fraction of Satellites Involved in Outages (a) & Percentage of Outages by Maximum S_4 (b). Table 3.4 (a) shows that most outages involve a small fraction of satellites. Table 3.4 (b) shows that most simultaneous outages occur during weak scintillation. These statistics exclude satellites whose elevation is below 15°

(a)

Fraction of Available Satellites vs. All Outages (%)

Fraction of Satellites	Ascension	Ancon	Parepare	Marak Parak
0	0	0.02	0	2.42
0.1	57.62	52.86	46.04	92.34
0.2	23.22	11.01	7.69	4.71
0.3	1.85	0.91	0.71	0.03
0.4	0.42	0.82	0.26	0.03
0.5	0.88	1.87	0.39	0
0.6	0.3	1.35	0.52	0.03
0.7	0.66	1.11	1.53	0
0.8	2.92	6.31	8.48	0
0.9	0	0	0.39	0.03
1	12.12	23.73	33.98	0.4

(b)

Maximum S_4 vs. Simultaneous Outages (%)

S_4	Ascension	Ancon	Parepare	Marak Parak
0	55.69	55.57	61.53	0
0.1	29.46	20.39	18.1	50
0.2	3.35	9.92	5.07	16.67
0.3	2.46	5.14	3.38	16.67
0.4	2.12	3.37	2.75	0
0.5	1.34	1.68	2.36	0
0.6	1.79	0.94	1.64	8.33
0.7	0.89	1.31	1.5	0
0.8	0.11	0.65	0.97	0
0.9	0.33	0.19	0.43	0
1	2.46	0.84	2.27	8.33

- Outages are generally clustered around low elevation angles, with a second peak between 40-60° during ascent (Figure 3.6).
- Long duration outages are primarily confined to elevation angles $\leq 20^\circ$ (Figure 3.4).
- After removing outages $\leq 20^\circ$, the majority of the remaining outages are 10 min or less (Figure 3.7).
- Outages involving all satellites occur in as many as $\approx 34\%$ of the cases, and the majority of these simultaneous outages last two minutes or less and are associated with S_4 values below 0.3. This suggests phenomena other than scintillation at work (Table 3.4).

We said earlier in this section ignoring outages may lead to under-estimates in the intensity and frequency of scintillation. Consequently, we explored imputing values when we were reasonably certain the data gap arose because of scintillation. The observations above were used to build an algorithm that imputed missing S_4 values prior to any further calculations. The decision to embark on an imputation scheme, furthermore, was made with the understanding that any subsequent analysis using imputed data would require modifications to standard statistical measures [Little and Rubin, 2002], and that imputation has the potential to distort the data. In its final form the imputation scheme worked as follows:

1. Identify gaps in data lasting longer than 1 min, but less than 10 min. The upper limit of 10 min was based on the results after removing outages less than 20° .
2. Outages lasting longer than 10 min are ignored.
3. If the elevation of the missing satellite was last reported at or below 20° do not fill since this may be a mask-horizon problem or multipath.
4. If the elevation of the satellite before the outage was greater than 20° , assume scintillation and impute a value of 8.88 as a flag. Because we were concerned only with the number and fraction of satellites reporting S_4 above 0.3, 0.5 and

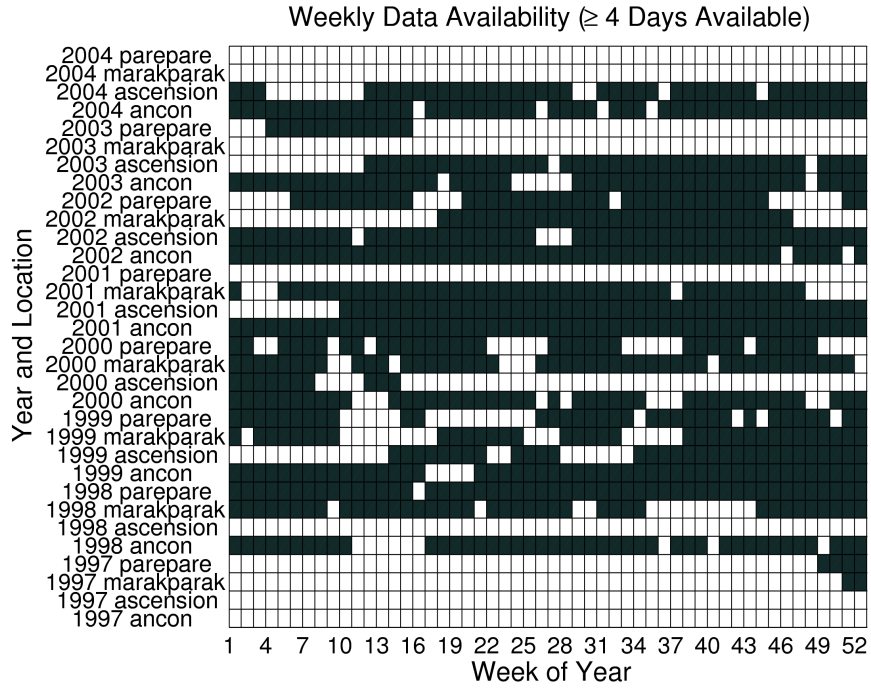
0.8, the 8.88 imputation value served to place the particular missing satellite in the highest bin, indicating severe scintillation.

At the end of our investigation, we attempted to confirm some solar-cycle, seasonal and diurnal behavior in the number and fraction of satellites scintillated. To do this, we combined data from various years, days and times in order to fill in the large scale gaps. This was a so called “hot-deck” imputation scheme in which missing values are filled with values from similar circumstances (e.g. same site, day of year, time, and solar-cycle conditions, but from a different year). In Figure 3.9 (a) each 7-day week of the year is plotted along the abscissa and each site and year combination considered is plotted on the ordinate. Black shading indicates at least 4 days of data in a given 7-day period are available. White shading indicates areas where data availability falls below that threshold. Figure 3.9 (b) shows the F10.7 cm solar flux values and identifies the site/year combinations chosen for analysis. A further description of the process used to select the data, and the types of calculations carried out is presented in Section 3.3.

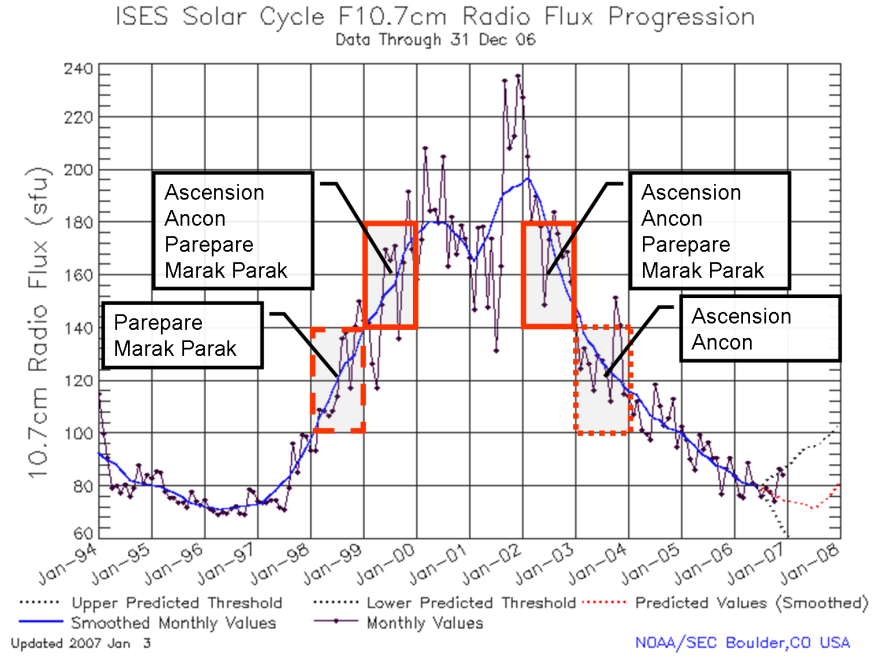
3.3 Data Processing

Our original objectives were: To determine the percent probability of occurrence of S_4 exceeding 0.3, 0.5 and 0.8 at the 50th, 75th and 95th percentile levels as a function of week and sunset-relative time, and determine the resulting effect on GPS horizontal dilution of precision, HDOP (see Subsection 2.1.4). We used **Matlab**® to process the data as follows:

1. Runs were conducted with and without imputation for comparison.
2. All times were adjusted to be relative to local sunset and “wrapped” (see below).
3. Seven days of S_4 values were collected and segregated into 15 minute “blocks”.
4. Counts were taken of the number of S_4 values exceeding the 0.3, 0.5 and 0.8 thresholds for a given time block for each of the seven days.



(a)



(b)

Figure 3.9: Large scale data gaps (a) and solar cycle relationships (b). White regions in (a) indicate missing data, black indicates at least 4 days of data are available in the corresponding week. In (b), the years chosen to be grouped together for each site are shown in relation to the solar activity as indicated by the F10.7 cm solar flux.

5. For each S_4 threshold, the data was sorted and the 50th, 75th and 95th percentiles calculated.
6. Resulting values were plotted by week and year.

Since we were concerned with nocturnal scintillation (section 2.2.2), the times were adjusted from UTC to local sunset for easy comparison between sites. For some locations, data spanned UTC midnight; in other words, a single night’s scintillation was spread over two UTC days. Consequently there was a portion of data in the early morning hours on a given UTC day, a large gap during daylight, then more data beginning in the UTC evening. For computational efficiency, rather than concatenating data records, the data prior to sunrise on a given UTC day was “wrapped” around to the end of that UTC day by adding 86400 s to the sunset-relative time stamps. For the computations above, this adjustment was transparent.

Collecting seven days of data in 15 minute “blocks” provided a maximum of 105 observations per satellite per block, assuming all observations were recorded or imputed. We also required 420 observations per block, arriving at this threshold by assuming at least four satellites were reporting over the seven day period; $4 \times 105 = 420$. When the total number of observations fell below 420, calculations were not performed and the block was skipped.

HDOP was calculated at one minute intervals for the same data. Initially, HDOP was calculated using all available satellites, regardless of S_4 value. Then satellites with S_4 values exceeding the thresholds above were incrementally removed and new HDOPs calculated. Recall from Chapter II in order to calculate HDOP, the satellite positions are required. However, for the imputed data, no position information was available. Consequently, almanac data⁴ were used in the following manner to calculate HDOP:

1. Almanac data were compiled for the particular day and times for which observational data was available, using code provided by Dr. John Raquet.

⁴subsection 2.1.2

2. The \mathbf{H} matrix ,Equation 2.7, was loaded with the positions of all satellites above a 20° mask.
3. If almanac output indicated a visible satellite that did not appear in the data, that satellite was assigned an S_4 value of 999.99.
4. HDOP was calculated for the following thresholds: All satellites regardless of S_4 , $S_4 < 0.8, 0.5$ and 0.3 . If less than four satellites were available, an HDOP value of -1 was assigned, indicating the inability to calculate HDOP.
5. All times were adjusted to be sunset relative and data was “wrapped around” as before. The effect of this “wrapping” will be apparent when one minute HDOP values are plotted.

At the end of our investigation, we also created summary plots of diurnal, seasonal and solar-cycle behavior using hot-deck imputation described in Section 3.2. The same percentiles and thresholds were used, but no one-minute imputation was carried out.

These procedures were scripted in `Matlab`[®] and applied to the data. Both the creation of the statistics and figure generation were automated to allow an investigator to choose any combination of sites and years to analyze. In the next chapter, we present the results of the investigation and corresponding images.

Table 3.5: Summary Plot Data Combinations showing years used and grouping of one-minute data. For the solar cycle comparison, individual years were analyzed. For the other comparisons, the data from all the years shown was combined. One-minute data was grouped into 15min blocks or simply combined. For the seasonal comparison, all weeks were treated individually. For the solar cycle and diurnal comparison, weeks 11-13 and 37-39 (centered on the equinoxes) were used.

	Solar Cycle	Seasonal	Diurnal
Ascension	2000	1999	1999
	2004	2002	2002
		2003	
Ancon	1998	1999	1999
	2001	2002	2002
		2003	
Parepare	1998	1998	1999
	2000	1999	2002
		2002	
Marak Parak	1999	1998	1999
	2001	1999	2002
		2002	
One Minute Data	15-min block	all	15-min block
Weeks	11-13 & 37-39	Individual	11-13 & 37-39

IV. Results and Analysis

NOW we examine the statistics generated using the procedures presented in Chapter III. We investigate the solar cycle, seasonal and diurnal behavior described in Chapter II. This analysis is carried out for both raw and imputed data. One-minute HDOP results are evaluated. Finally, we scrutinize the imputation results. Before embarking on this journey, however, we briefly present some examples of our work and provide a commentary on interpreting the output.

In Section 3.3 we said we were going to examine the percent probability of occurrence of exceeding three S_4 thresholds at three percentile levels. The S_4 thresholds chosen were 0.3, 0.5, and 0.8 and represent weak–moderate, moderate–strong and extreme levels of scintillation. The 50th (also called the median), 75th (also called the upper quartile), and 95th percentiles were chosen. *Wilks* [1995] provides the following interpretation of percentiles:

A sample quantile [percentile] q_p is a number having the same units as the data, which exceeds that proportion of the data given by the subscript p with $0 \leq p \leq 1$. The sample quantile q_p can be interpreted approximately as the data value exceeding a randomly chosen member of the data set, with probability p . Equivalently, the sample quantile q_p would be regarded as the $[p \times 100]^{\text{th}}$ percentile of the data set.

Stated another way, there is a $(1 - p) \times 100$ percent chance that a randomly sampled value would exceed that found at the $[p \times 100]^{\text{th}}$ percentile of the data set. Figure 4.1 provides an example for discussion. Figure 4.1 is a plot of the percentage of available satellites (indicated on the ordinate) being scintillated with $S_4 > 0.5$ as a function of hours after local sunset (indicated on the abscissa) for Ascension in 2001 during week 11. The data has been sorted into 15-minute bins as described in Section 3.3 and no imputation has been carried out. Three lines represent the percentage of satellites at the 50th (heavy solid line), 75th (dash-dot line) and 95th (thin solid line) percentiles. Four hours after local sunset we can see that at the 50th percentile, slightly under 35% of the available satellites can be expected to have an $S_4 > 0.5$. At the 75th percentile, about 4.5 h after local sunset, the number of

satellites reporting $S_4 > 0.5$ is 60% while at the 95th percentile the value climbs to approximately 89%. This is expected since, as noted in Section 3.2, high values of S_4 typically affect a small percentage of satellites.

In addition to weekly plots, we also constructed yearly summary plots. Figure 4.3 is an example. In Figure 4.3, the abscissa indicates the sunset relative time as before, however the ordinate now shows week-number. The colors represent the various fractions of satellites affected by scintillation at the particular S_4 and percentile combination. In this figure, the median (a), upper quartile (b) and 95th percentile (c) for $S_4 > 0.3$ are displayed. The white areas indicate insufficient data. As before, no imputation was carried out. The striations that run from the upper left to lower right of the figure are a result of the precession of the GPS satellites. Each day the satellite arrives four minutes earlier than the day before; the number of available satellites change in regular patterns throughout the year. These figures show the same increase in the fraction of affected satellites with increasing percentile level. In short, the combination of high percentile and low S_4 threshold will produce the most dramatic results. Consequently, the bulk of subsequent figures will have an S_4 threshold of 0.3 at the 95th percentile.

4.1 *Solar Cycle Comparison*

Recall from Table 2.2.2 the production of EPBs and resulting scintillation tends to mirror the solar cycle. In Figure 4.4 shows the solar cycle sensitivity for Ascension (a), Ancon (b), Parepare (c) and Marak Parak (d). These plots depict the fraction of available satellites experiencing $S_4 > 0.3$ at the 95th percentile as a function of hours after local sunset. For each site, years for comparison were selected near solar maximum and solar minimum as indicated in Figure 3.9 (b). For all the sites in Figure 4.4, the influence of the solar cycle is apparent. The effect is most pronounced at the Appleton Anomaly crest stations of Ascension (a) and Parepare (c), although the fraction of affected satellites jumps as much as 30% at the geomagnetic equator

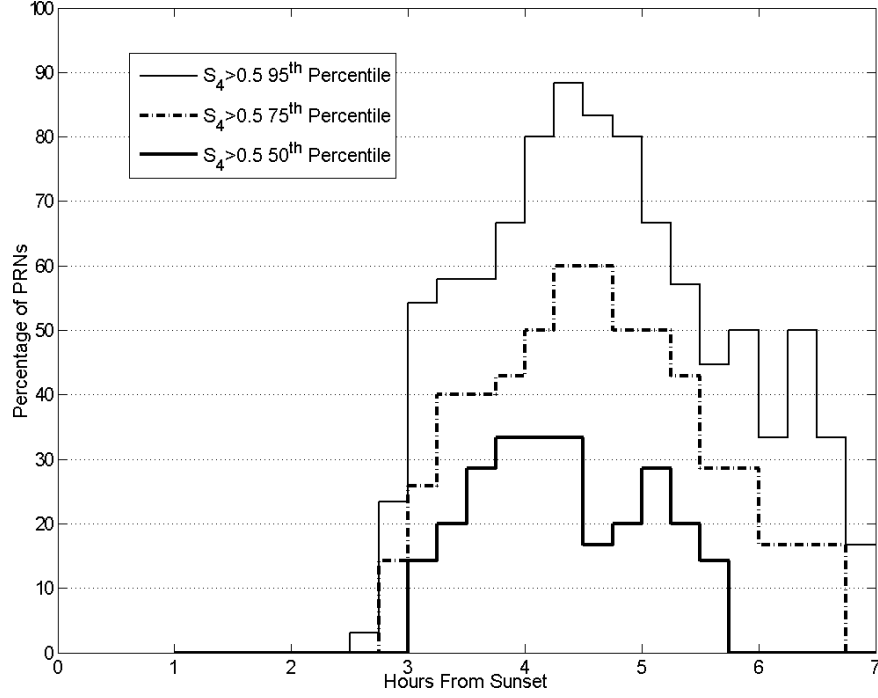


Figure 4.1: Ascension 2001, Week 11, Percentage of Satellites with $S_4 > 0.5$ at the 50th (heavy solid line), 75th (dash-dot line) and 95th (thin solid line) percentiles. This figure was created using raw data.

stations. This is consistent with the behavior presented in Table 2.2.2 which noted the bubble activity was highest under the anomaly crests.

We also examined the impact on the results using our imputation scheme described in Section 3.2. Figure 4.5 shows the comparison for Parepare during 1998 (a) & (c) and 2000 (b) & (d). In this example, (a) and (b) represent the raw data, while data gaps in (c) and (d) were imputed. The abscissa indicates the hours after local sunset; the ordinate indicates the week number. The color scale represents the fraction of available satellites with $S_4 > 0.3$ at the 95th percentile. Again the solar cycle influence is apparent, with much higher values appearing in 2000 during the solar maximum, particularly during the spring equinox. The impact of the imputation scheme is less obvious, although close inspection will reveal enhanced values between weeks 30 and 35 and during week 40 for the 1998 data (Figure 4.5 (a) and (c)). The impact of imputation will be discussed in greater detail in Section 4.5.

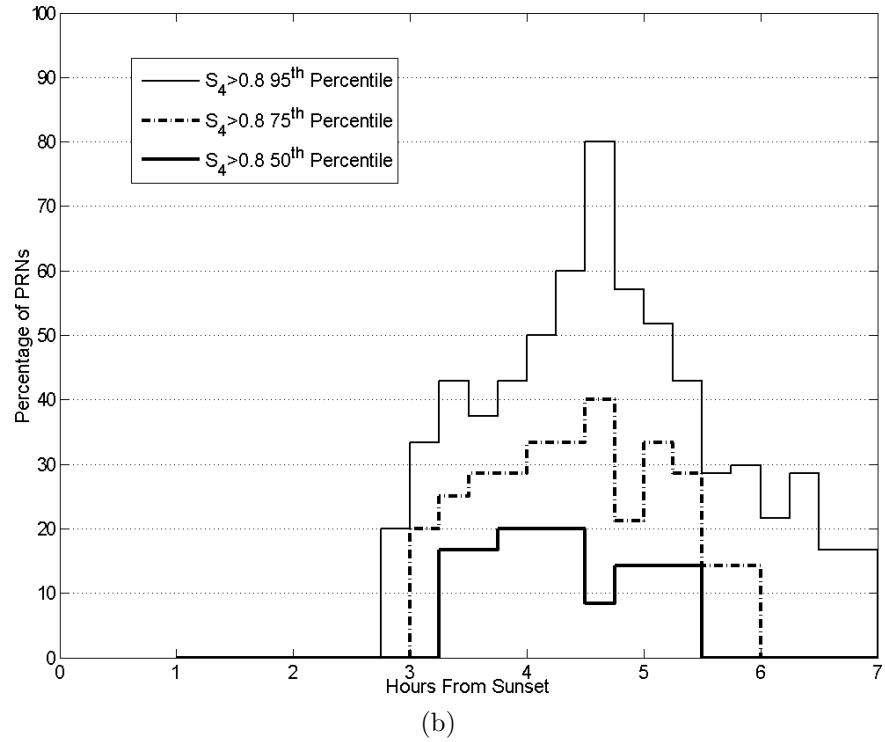
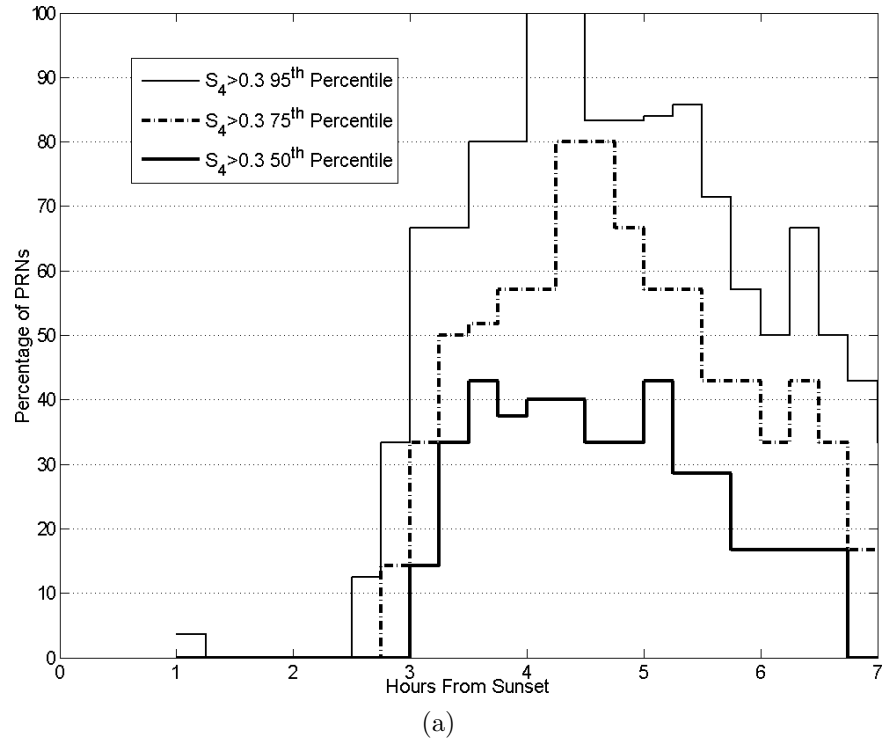


Figure 4.2: Ascension 2001, Week 11, Percentage of Satellites with $S_4 > 0.3$ (a) and $S_4 > 0.8$ (b). These figures were created using raw data.

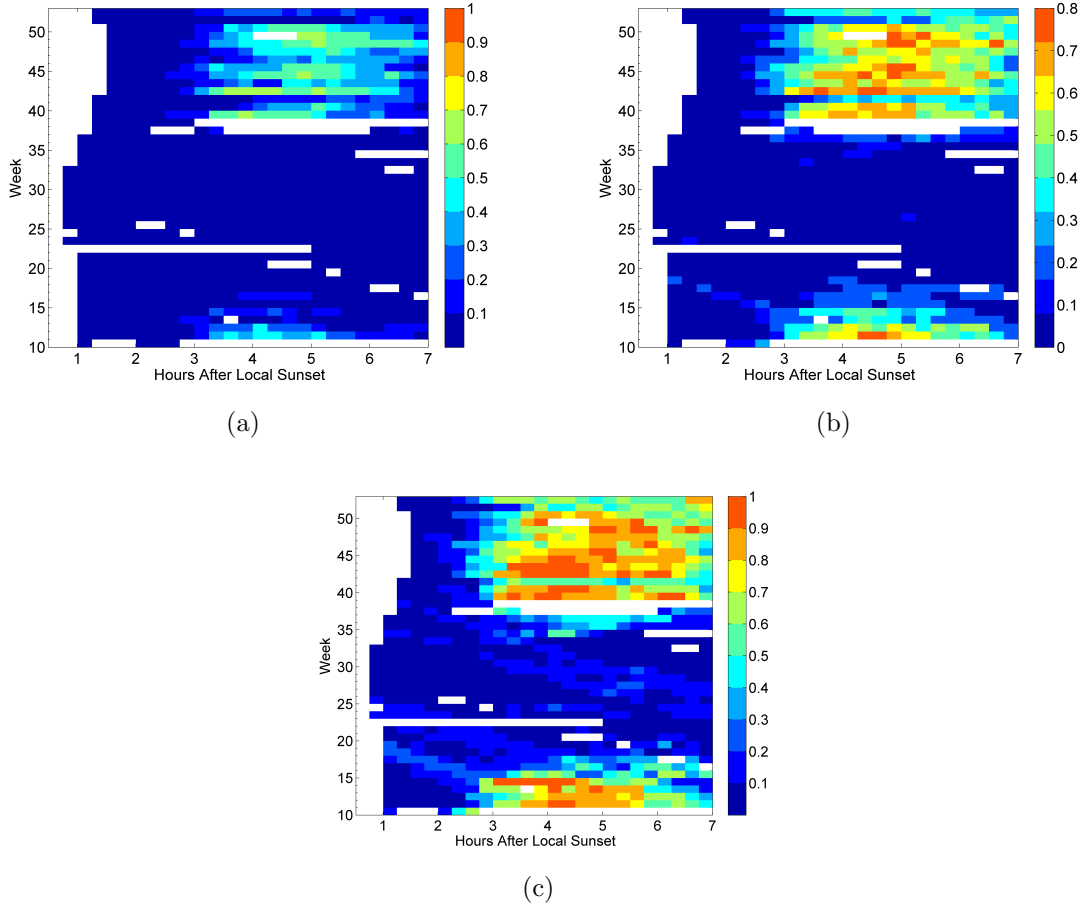
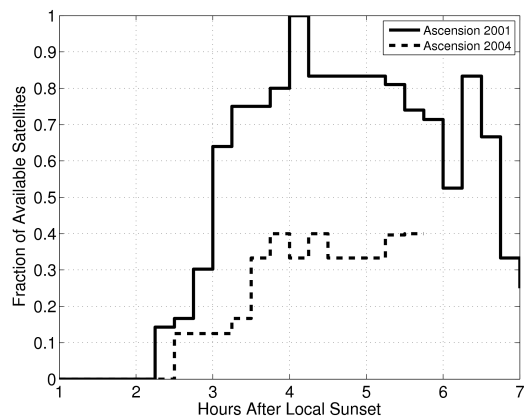
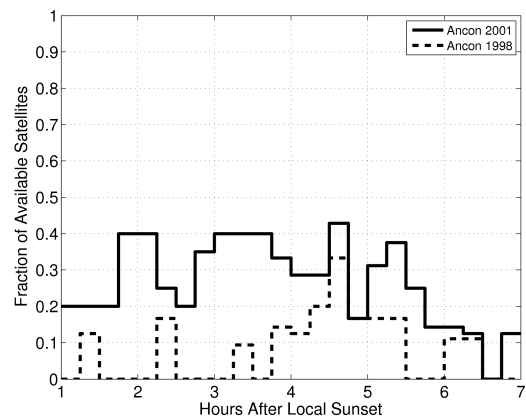


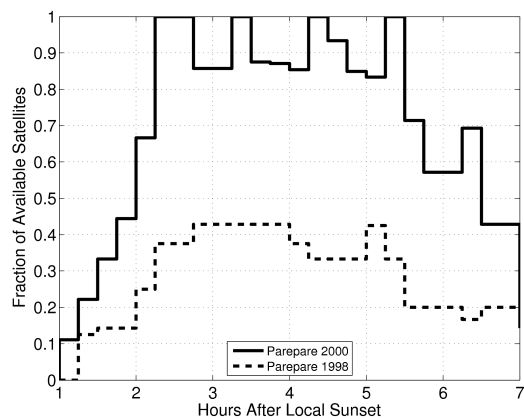
Figure 4.3: 2001 Summary for Ascension, Ratio of satellites with $S_4 > 0.3$ to all available, 50th (a), 75th (b), and 95th (c) Percentile. The abscissa indicates the hours after local sunset; the ordinate indicates the week number. Striations running from upper left to lower right are an artifact of GPS precession: the number of satellites available changes in regular patterns throughout the year. These figures were created using raw data.



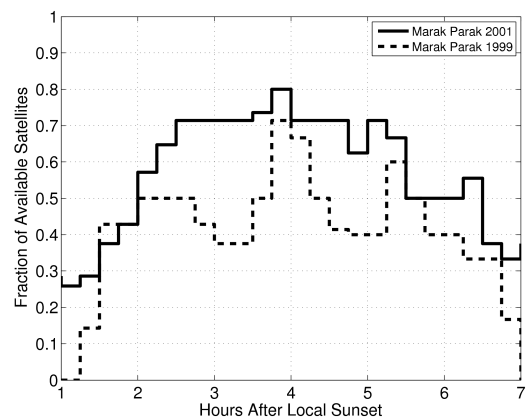
(a)



(b)

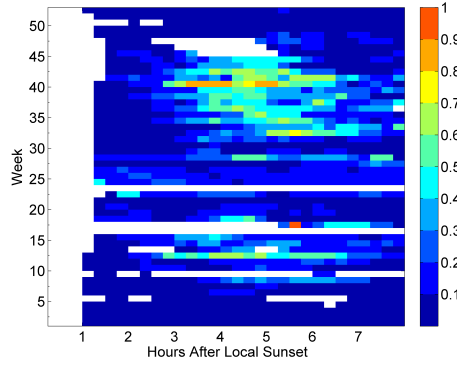


(c)

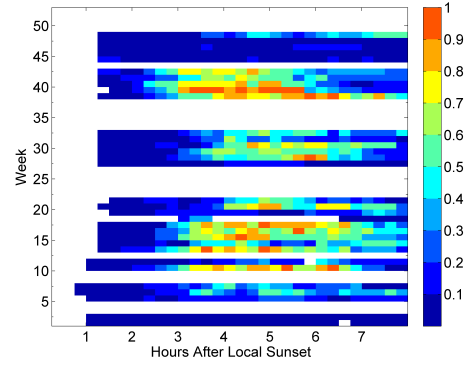


(d)

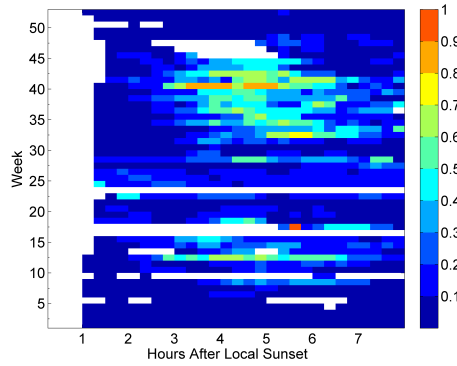
Figure 4.4: Solar cycle sensitivity for Ascension (a), Ancon (b), Parepare (c) and Marak Parak (d). These plots depict the fraction of available satellites with $S_4 > 0.3$ at the 95th percentile as a function of hours after local sunset. The abscissa indicates the hours after local sunset; the ordinate indicates the week number. These figures were created using raw data



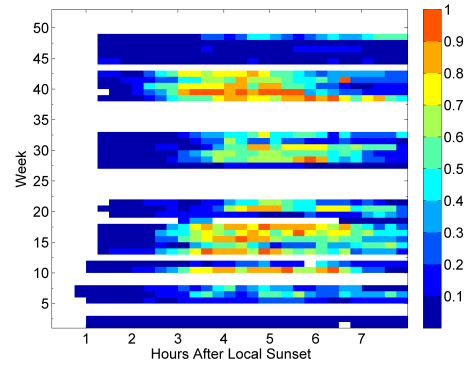
(a)



(b)



(c)



(d)

Figure 4.5: Solar Cycle Comparison Parepare for 1998 (a) & (c) and 2000 (b) & (d). Raw data was used for (a) and (b) while (c) and (d) were filled using the imputation scheme described in Section 3.2

4.2 Seasonal Comparison

Figure 4.6 shows the results of a seasonal comparison using data from the years identified in Table 3.5. Like the earlier figures, the values on the ordinate represent the fraction of available satellites experiencing S_4 levels above 0.3 at the 95th percentile at the four sites. The abscissa, however, now indicates the week number. Both the data (markers) and the smoothed results (solid lines) were plotted. The smoothed results were created by applying a five-week boxcar-average to the raw results. Other than the “hot deck” imputation carried out by combining the different years, no other imputation was performed.

In Figure 4.6, the equinox activity peaks described in Table 2.2.2 are evident, although the onset and cessation of the enhanced scintillation is not precisely centered on the equinox. Ascension’s activity seemed to reach its zenith on the equinox, while Parepare’s was delayed by 2–3 weeks. At the geomagnetic equator, Ancon’s maxima appeared to occur around week 6, while Marak Parak did not reach its spring peak until week 21. The response was more uniform around the autumnal equinox with all sites showing a peak in activity. Unlike the spring, Marak Parak showed a well-defined maximum and was the closest to the autumnal equinox. The maximum levels at Ascension and Parepare were almost simultaneous, while Ancon lagged behind. The amplitude of the seasonal cycle was higher for the anomaly crest stations, but all reflected the solstitial lull.

Figure 4.7 is the seasonal comparison for Ascension showing the fraction of satellites with $S_4 > 0.3$ at the 95th percentile. The abscissa indicates the hours after local sunset; the ordinate indicates the week number. Figure 4.7 (a) shows the results for the raw version, while (b) shows the results for the imputed version. The equinox peaks mentioned in the preceding paragraph are visible in both the imputed and raw versions, although the fall equinox values are somewhat enhanced in the imputed version. Here $S_4 \geq 0.3$ affects *all* available satellites and lasts for over an hour during weeks 14, 42–45.

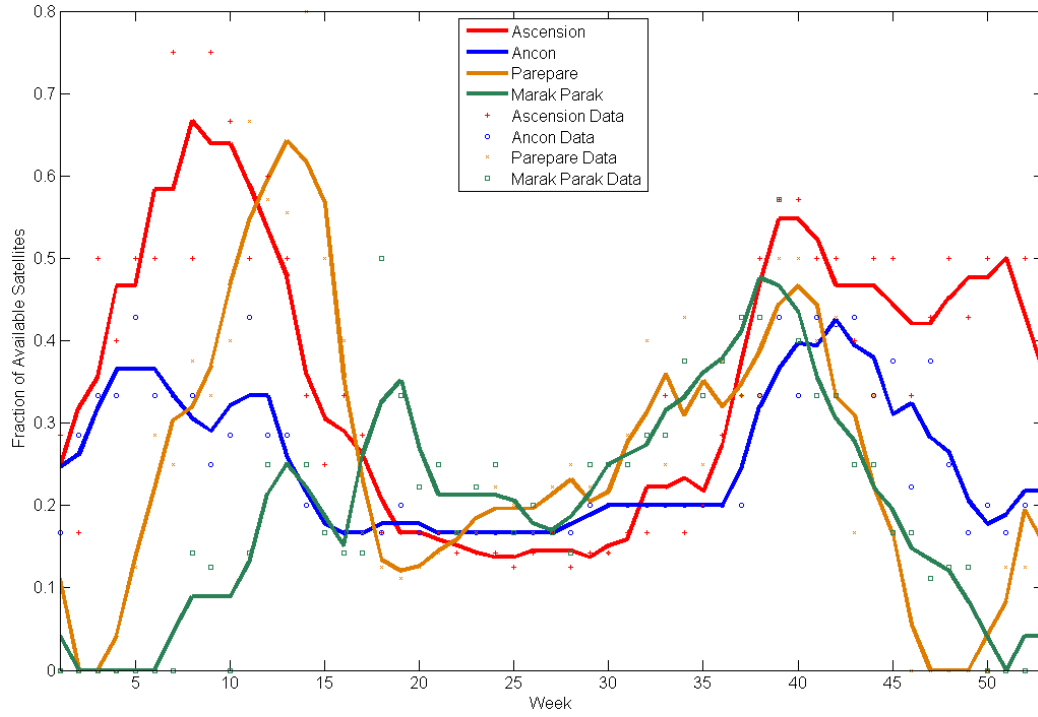
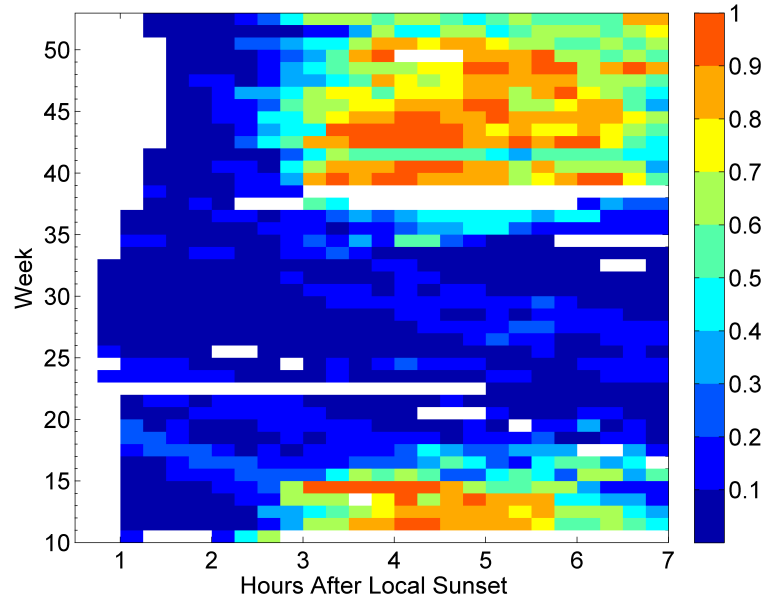
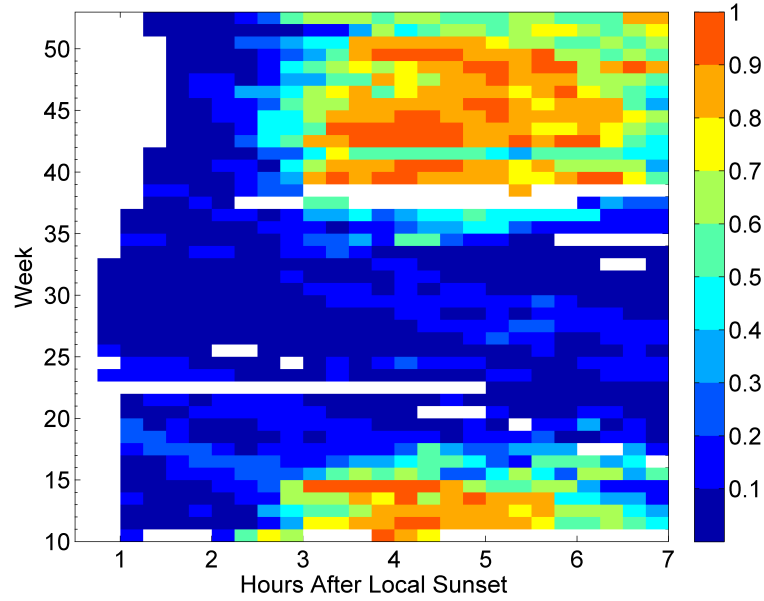


Figure 4.6: Seasonal Comparison for Ascension, Ancon, Parepare, and Marak Parak; fraction of satellites with $S_4 > 0.3$ at the 95th percentile. Solid lines represent the results when a 5-week filter was applied to the results. The original data points are indicated by the markers.



(a)



(b)

Figure 4.7: Seasonal Comparison for Ascension showing the fraction of satellites with $S_4 > 0.3$ at the 95th percentile. The abscissa indicates the hours after local sunset; the ordinate indicates the week number. Figure 4.7 (a) shows the results using raw data, while (b) shows the results using the imputation scheme described in Section 3.2.

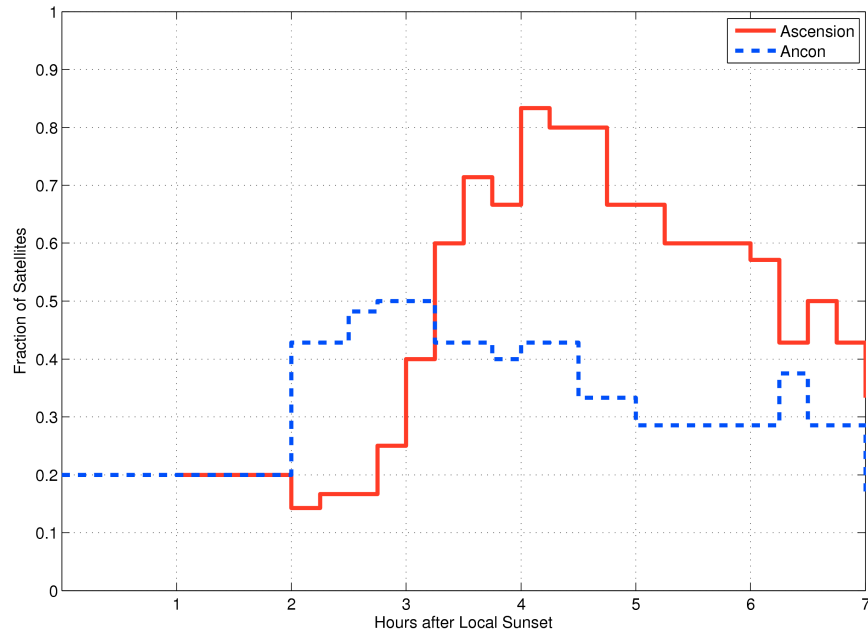
4.3 Diurnal Comparison

Recall in Table 2.2.2 the diurnal cycle was characterized by the onset of EPB and scintillation activity about an hour after local sunset, a peak around 2200L and dissipation by sunrise. Figure 4.8 shows the diurnal behavior for Ascension and Ancon (a) and Parepare and Marak Parak (b), using data from the years identified in Table 3.5. These ordinate indicates the fraction of available satellites with $S_4 > 0.3$ at the 95th percentile as a function of hours after local sunset indicated on the abscissa. *de La Beaujardiere et al.* [2004] notes that begins at the anomaly crest stations sixty to ninety minutes later than the equatorial stations. She attributes this to "... a finite upwelling speed of the irregularities at the magnetic equator." This behavior is most evident in the Atlantic & Americas longitudinal sector stations, Figure 4.8 (a), where the ramp-up of activity occurs about three hours after local sunset at Ascension, while the increase at Ancon occurs at the two-hour point. In the Pacific longitudinal sector, however, the lag appears to be 15 to 30 minutes. This may be attributed to the relative differences in location. Ascension and Ancon are widely separated by latitude and longitude, while Parepare and Marak Parak are at essentially the same longitude (see Figure 3.1. Also, Table 3.1 shows that Ancon is closer to the magnetic dip equator than Marak Parak.

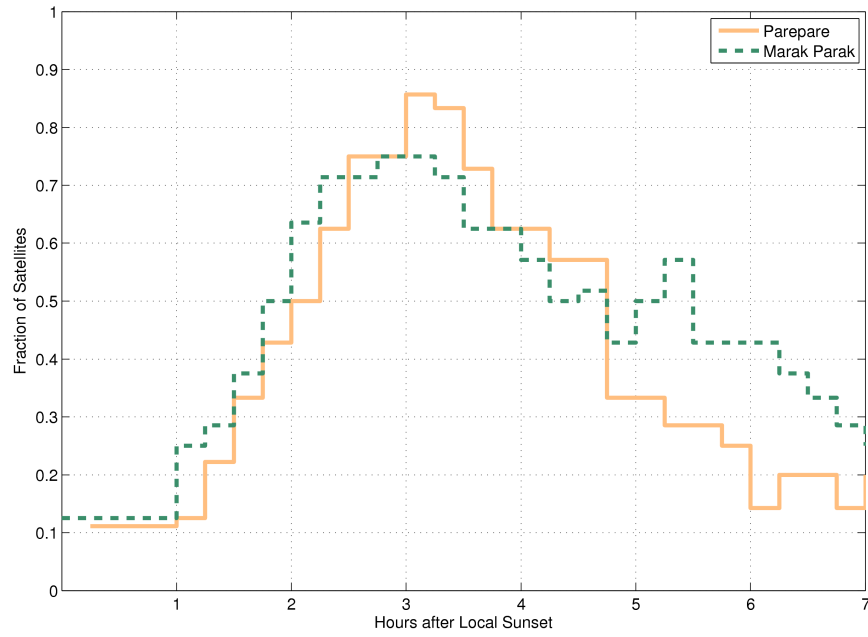
Figure 4.9 shows the diurnal cycle at Parepare for week 13 during 2000 for the median, upper quartile and 95th percentile. The ordinate is now the *number* of satellites with $S_4 > 0.3$, and the abscissa, as before, is the hours from local sunset. Figure 4.9 (a) shows the raw results, while (b) shows the imputed results. The diurnal cycle is again well represented, and the influence of imputation is more apparent. At the median level, there are times when the number of satellites affected by $S_4 > 0.3$ rises to three in the imputed case, from two in the raw version.

4.4 Annual Horizontal Dilution of Precision (HDOP) Summaries

HDOP calculations were made using the technique described in Section 3.3. Figure 4.10 shows the results for Ascension in 2001 using raw one-minute data. Fig-

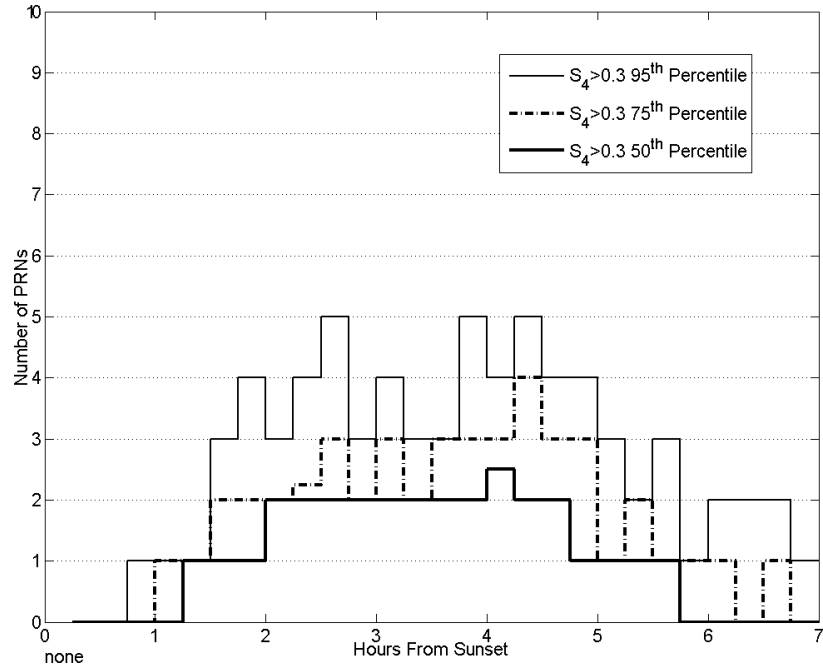


(a)

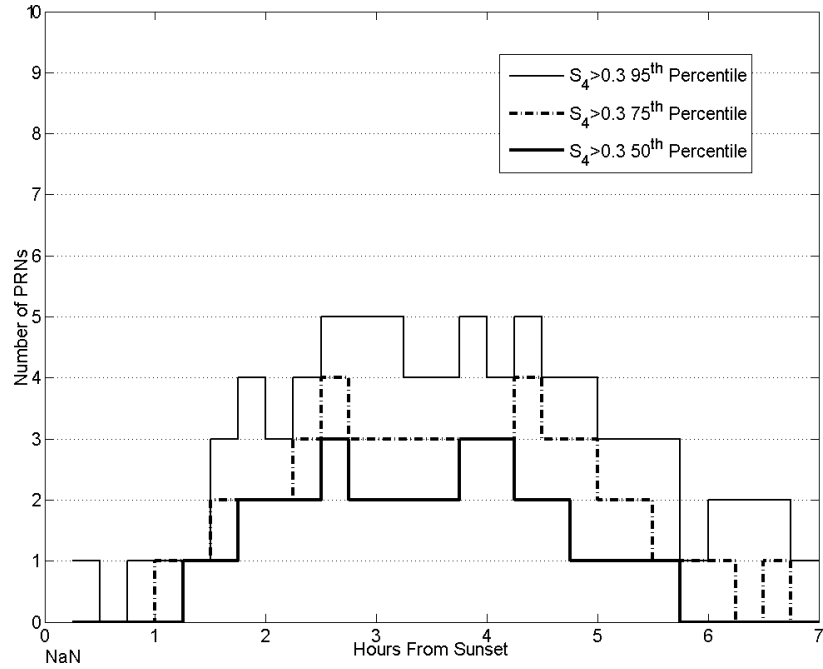


(b)

Figure 4.8: The diurnal behavior for Ascension and Ancon (a) and Parepare and Marak Parak (b), using data from the years identified in Table 3.5. These ordinate indicates the fraction of available satellites with $S_4 > 0.3$ at the 95th percentile as a function of hours after local sunset, which is indicated on the abscissa.



(a)



(b)

Figure 4.9: Diurnal Comparison, Parepare week 13, 2000, raw (a) and imputed (b) results. The diurnal cycle at Parepare for the median, upper quartile and 95th percentile. The ordinate is now the *number* of satellites experiencing $S_4 > 0.3$, and the abscissa, as before, is the hours from local sunset.

Figure 4.10 (a) shows HDOP obtained assuming no scintillation but using only satellites shown in the data, as opposed to all satellites indicated by the almanac. Consequently, some periods where HDOP could not be determined are still evident. Figures 4.10 (b) through (d) show the results after removing all satellites with an $S_4 > 0.3$, 0.5 and 0.8 respectively. The ordinate in this case is the day of year, and the abscissa is the time after local sunset. The color bar indicates the HDOP value. Recall from Chapter II that $HDOP = 1$ is considered perfect. The white spaces indicate missing data while the gray shading indicates the inability to calculate HDOP because less than four satellites were available below the particular S_4 threshold. As the S_4 threshold increases from (c) to (d) and the number of available satellites increases, notice how the HDOP values drop and amount of gray shading diminishes. In Figure 4.11 we have plotted the relative difference in HDOP between the $S_4 > 0.3$ threshold case Figure 4.10 (b) and the case in which no scintillation was occurring Figure 4.10 (a). The largest relative changes (i.e. 1) are coincident with the areas of gray shading in Figure 4.10 (b) where no solution was available. Less dramatic yet still substantial changes are peppered around these areas in Figure 4.11.

4.5 Imputation Performance

Figures 4.12 (a) and (b) depict the occurrence of differences in the fraction of scintillated satellites between imputed and raw results for Ascension in 2001. The abscissa is hours past sunset and the ordinate is the week. Figure 4.12 (a) shows the occurrence of differences between the imputed and raw results at the median for the fraction of satellites with $S_4 > 0.8$, while (b) shows the 95th percentile for the fraction of satellites with $S_4 > 0.3$. The changes are confined to the equinox peaks in (a), while in (b) the seasonal clusters are ill-defined and changes begin to appear in the off-season as well. Similar results were obtained for Parepare (not shown), although the correlation are not as compact. These comparisons were made during the solar maximum. During solar minimum (not shown), the patterns are more diffuse, with fewer difference between raw and imputed percentages. Ascension and Parepare are

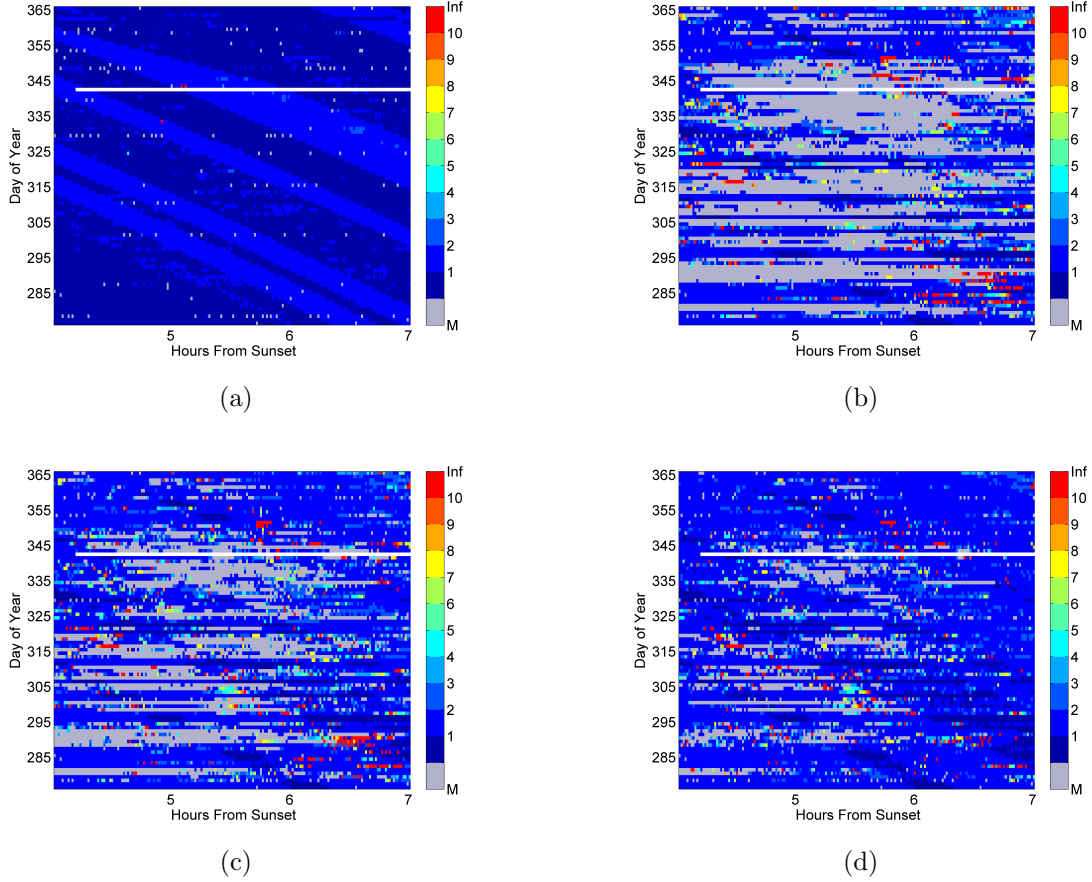


Figure 4.10: HDOP Comparison: HDOP results without any satellites removed for scintillation is shown in Figure 4.10 (a) while Figure 4.10 (b) through (d) show the results after removing all satellites with an $S_4 > 0.3$, 0.5 and 0.8 respectively. The ordinate in this case is the day of year, and the abscissa is the time after local sunset. The color bar indicates the HDOP value (recall from Chapter II that a value of 1 is considered perfect.) Gray areas indicate times when less than four satellites were available, and hence no navigation solution, or HDOP calculation, was available.

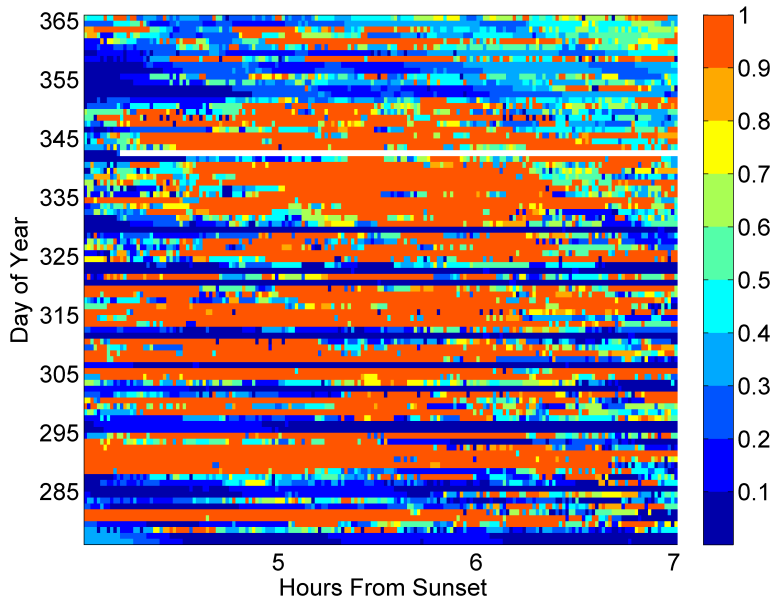


Figure 4.11: 4.11 is the relative difference in HDOP between the $S_4 > 0.3$ threshold Figure 4.10 (b) and the case in which no scintillation was occurring Figure 4.10 (a).

both situated under the anomaly crest. We examined Ancon and Marak Parak (not shown), closer to the geomagnetic equator. Here the seasonal correlation was much harder to discern, particularly during solar minimum. Based on an examination of plots like those shown in Figure 4.12, the performance of the imputation scheme appears to deteriorate as percentile increases and S_4 and solar activity decrease. To gain a better understanding of the magnitude of the difference between the imputed and raw results, we performed a simple hypothesis test. For each of the 32 15-min blocks, for each week at a given location, year, percentile and S_4 threshold, we calculated the difference d_i between the imputed and raw results. If there was no significant difference between the raw and imputed results, the mean of their differences, μ_d should be zero. If $\mu_d \neq 0$, the imputation scheme had a statistically significant impact. This can be expressed as a null and alternative hypothesis as:

$$H_0 : \mu_d = 0$$

$$H_a : \mu_d \neq 0$$

We chose a Z-test on the mean of the differences μ_d at the $\alpha = 0.05$ significance level. In order to apply the test, we had to ensure the samples were independent. We examined the lag-1 autocorrelation for the differences and found the overwhelming majority ($> 84\%$) of the samples were independent. Reasonably reassured by the autocorrelation results, we applied the Z-test to all sites, percentiles and S_4 levels during solar minimum and solar maximum. In all cases we were able to reject the null hypothesis at the $\alpha = 0.05$ significance level, meaning there was a statistically significant difference between the imputed and raw versions. The results are tabulated in Appendix B and show the maximum of the 95% confidence interval for the mean reached 14%, however values were typically less than 10%. A scatter plot of the hypothesis test results showed the highest mean differences were typically near the equinoxes, as expected. Our analysis suggests that the imputation scheme can produce statistically significant, albeit small, differences in the fraction of satellites scintillated.

In order to strengthen the imputation scheme and remove anomalous off-season results, we added a lower limit of 0.3 for minimum S_4 in the minute before an outage for a particular PRN and relaxed the duration limit to 20 min from the 10 min limit originally described in Section 3.2. We added the S_4 threshold to ensure the satellite was at least experiencing weak scintillation before an outage. We expanded the time limit to 20 min because a substantial number of the outages of this duration were present even after removing the outages below 20° (see e.g. Figure 3.7 (a)). This refinement produced the results shown in Figure 4.13 (a) and (b). Note the disappearance of off-season (solstitial) changes in Figure 4.13 (b) when compared to Figure 4.12 (b). The number of time-blocks that increased from the raw version also rose as seen in the appearance of additional + symbols around the equinox peaks in both Figure 4.13 (a) and (b). We conducted a Z-test on the means of the differences as we did for the original scheme. The confidence interval limits for the mean of the differences were generally lower for this imputation scheme than for the original for the solar minimum years and the geomagnetic equator locations (Ancon and Marak Parak). The confidence interval limits generally increased during solar

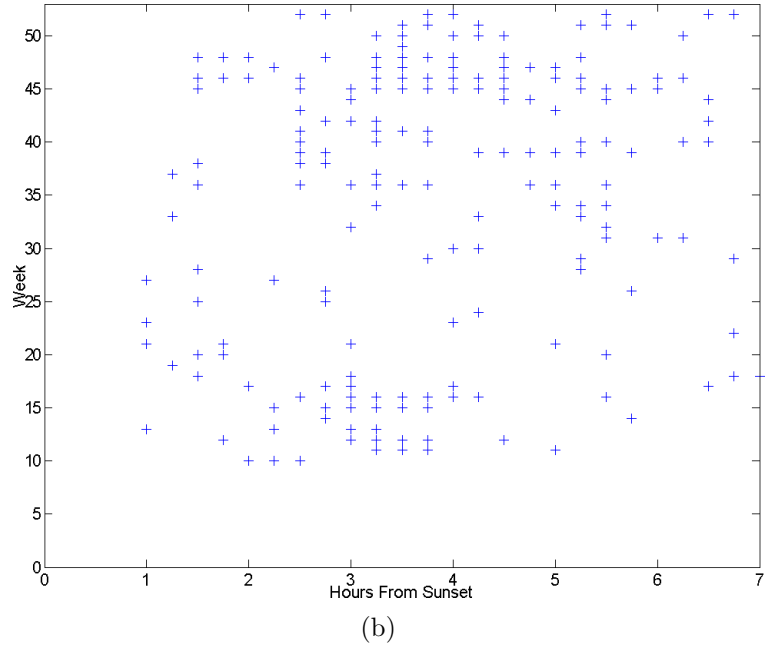
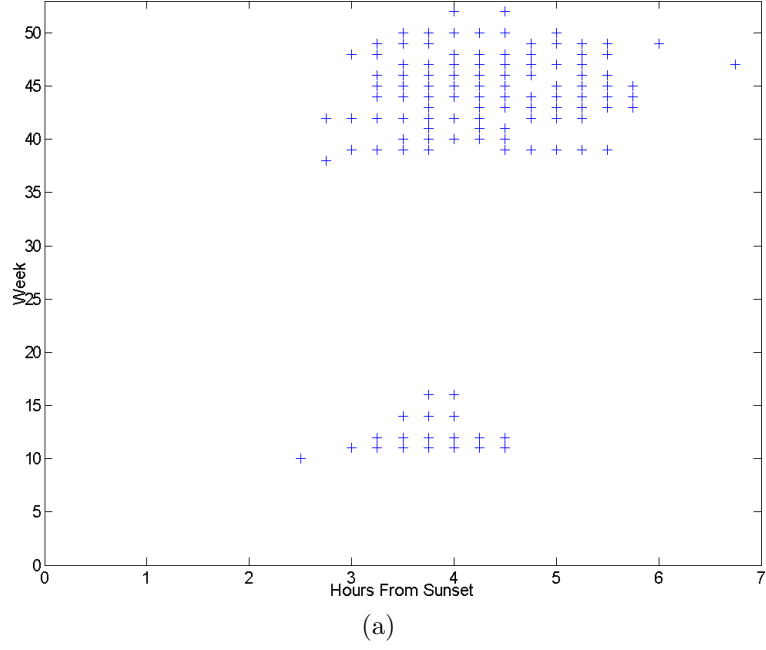


Figure 4.12: Difference between Imputed and Raw data at Ascension in 2001 using imputation criteria originally described in Section 3.2. The '+' indicates an increase over the raw data. Figure 4.12 (a) shows the difference at the median for $S_4 > 0.8$ while Figure 4.12 (b) shows the result at the 95th percentile for while for $S_4 > 0.3$. As in earlier figures, the abscissa indicates the sunset-relative time while the ordinate indicates the week of the year.

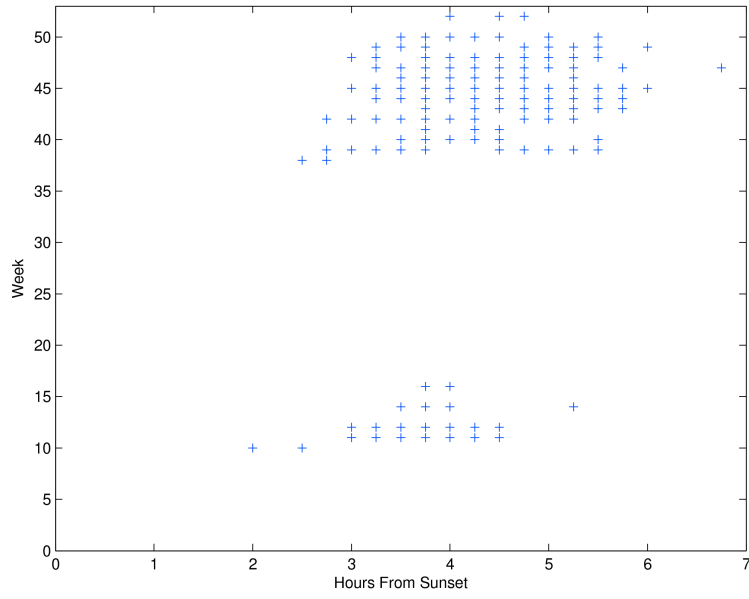
maximum at the anomaly crest locations (Ascension and Parepare). Additionally, the confidence interval peaks were more concentrated around the equinoxes than in the original scheme. Appendix B contains the comparison. These results suggest including an S_4 threshold and loosening the duration constraint produces more realistic output, opening the door for further refinement of the imputation scheme. Finally, we increased the S_4 threshold to 0.8 for a particular satellite prior to an outage, guaranteeing that any satellite for which missing values were imputed was experiencing severe–extreme scintillation in the minute prior to being lost. The results (not shown) were very similar to those using the 0.3 thresholds, although the Z–test confidence intervals were in some cases 1–2% lower. This further increased our confidence in the modified imputation scheme.

4.6 Summary

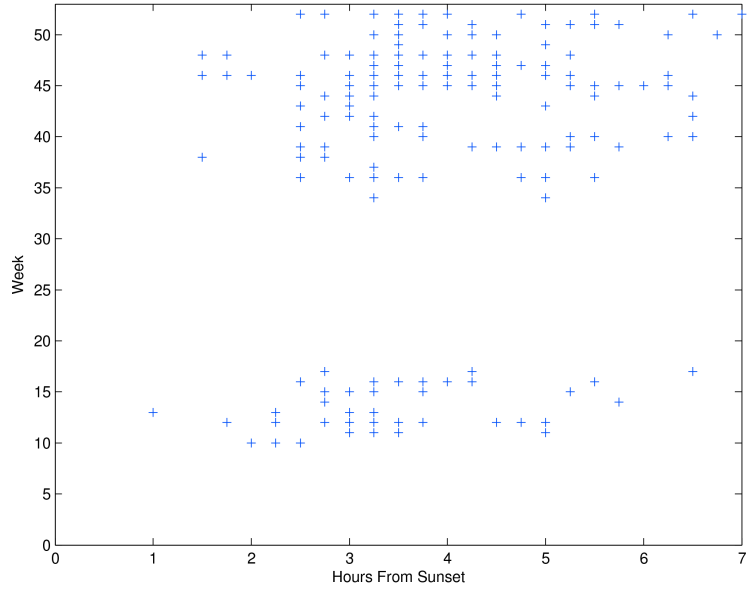
Thus we have been able to continue the work begun by *Thomas et al.* [2001], expanding it to include stations in the Atlantic and Americas sector, as well as exploring solar cycle influences. We were able to observe the behavior described in Chapter II in most cases with the following exceptions:

- The seasonal behavior during the spring at Marak Parak was peculiar, with the peak activity delayed until approximately week 21.
- In general the seasonal peaks were near, but not necessarily centered on the equinoxes at the four sites studied.
- The diurnal onset of scintillation conditions at the anomaly crest site at Parepare appeared to lag Marak Parak by only 15–30 min, rather than the 60–90 min we expected. The delay was about an hour in the Atlantic sector. The variation is most likely caused by the relative differences in location.

The HDOP plots clearly show the impact of scintillation on GPS precision. As satellites are removed based on S_4 thresholds, the HDOP increases and in extreme



(a)



(b)

Figure 4.13: Difference between Imputed and Raw data at Ascension in 2001 after adding a lower limit of 0.3 for maximum S_4 in the minute before an outage and relaxing the duration criteria to 20 min from the 10 min criteria originally described in Section 3.2. The '+' indicates an increase over the raw data. Figure 4.13 (a) shows the difference at the median for $S_4 > 0.8$ while Figure 4.13 (b) shows the result at the 95th percentile for while for $S_4 > 0.3$. As in earlier figures, the abscissa indicates the sunset-relative time while the ordinate indicates the week of the year.

cases, a navigation solution becomes impossible because less than four satellites remain. This result has serious ramifications for GPS users.

Finally, we saw that the imputation scheme increases the observed fraction of scintillated satellites at a typically small ($< 10\%$) yet statistically significant level and that the scheme can be improved by including an S_4 threshold and relaxing the duration constraint. All that remains for this work is a summation and recommendations for the future, which are presented in the next chapter.

V. Summary and Conclusions

WE have extended the work of *Thomas et al.* [2001] incorporating new sites and years. Additionally, a simple ad-hoc imputation technique was developed, tested and refined. The synoptic behavior that emerged from our analysis was consistent with the findings of other researchers. Choosing to study S_4 values collected during the solar maximum and at locations beneath the Appleton Anomaly crest resulted in some eye-opening images and statistics. That GPS could be unavailable to a military user for an hour or more is significant, particularly if operation is planned without accounting for scintillation. Even if GPS is available, precision may be severely degraded. It is important to remember, also, that the data for this research was collected with fixed receivers designed to track through moderate severe scintillation. Combat seldom provides such a favorable environment for either the equipment or the GPS user [*Thomas et al.*, 2001].

We had the advantage of comparing scintillation activity across the solar cycle. As anticipated, there was much more activity during the solar maximum at all stations, but again particularly at the anomaly crests in both longitude sectors. During the years closer to the solar minimum, activity was diminished, but still significant. We were also able to observe some departures from anticipated behavior at seasonal and diurnal time scales. We also discovered in the diurnal comparisons, a longitudinal difference in anomaly crest onset delay when compared to equatorial stations. The HDOP information we produced provides a bridge from relatively esoteric S_4 data to operationally applicable dilution of precision information. This is perhaps the most valuable portion of our research for the warfighter.

In an effort to gain a better estimate of scintillation and its operational impacts, we attempted an imputation scheme. While enabling us to “fill in the holes” and attempt to capture the true magnitude of the scintillation problem, the algorithm appeared over zealous when confronting low S_4 thresholds and high percentile levels. In light of these findings, we included a minimum S_4 threshold to further separate scintillation induced outages from non-scintillation outages. We also relaxed the out-

age duration limit to 20 min to capture more outages. The results were promising, producing patterns of change over raw data that were more realistic. Even after applying a very stringent minimum S_4 threshold of 0.8, the outcome was consistent, increasing our confidence in the scheme.

Finally, to our knowledge this was the first exploration of the patterns of “missingness” occurring in the S_4 data. We were able to turn missing data into “*missingness*” data by examining the circumstances surrounding the gaps. We believe the outages may represent another way of investigating scintillation, a means toward improving imputation schemes, and a potential climatological aid for planners to apply operationally. This naturally leads us to a discussion of future work.

5.1 *Future Work*

If further statistics are to be generated using imputation, more robust methods of dealing with missing data are needed. We introduced two apparent improvements to the imputation scheme and the results invite further investigation. A logical step could involve a more sophisticated scheme that capitalizes on the hole–boundary correlations between maximum S_4 and $\sigma_{S_4}^2$ to impute more realistic S_4 values.

As imputation is improved, other years and stations in the dataset await perusal. Continued study and updating of the information gathered by the SCINDA network is encouraged, along with the generation and maintenance of statistics such as those presented here. The data should be subjected to more robust statistical techniques, such as principal component analysis, to search for potential relationships among various stations and variables. The HDOP statistics in this research were produced using coarse almanac data. Precise ephemerides can provide the means to develop more accurate statistics. Since the HDOP statistics generated were at one-minute resolution, it might be instructive to calculate statistics at a 15 minute resolution for each week, as we did with the availability data.

The synoptic climatology of outages could also be examined. To our knowledge, no such research has been conducted using data from GPS receivers. Rather than attempting to fill-in missing data, it may be instructive to begin developing statistics related to the temporal and spatial patterns of missingness. This should be done not only for the types of receivers currently being employed in the SCINDA network, but also for typical receivers used by the civilian and military community. Such research may make it easier to raise awareness of ionospheric impacts on GPS.

In addition to work in and among the stations in the SCINDA network, comparisons can be made between SCINDA data and remote sensing data collected by platforms such as C/NOFS. *de La Beaujardiere et al.* [2004] notes that C/NOFS will be monitoring lightning, which has been linked to “explosive equatorial spread F” [*Woodman and Kudeki*, 1984]. Lightning data sets already exist and correlation between lightning and equatorial scintillation should be examined further.

Appendix A. Raw Data File Example

THIS appendix shows an example of a raw data file collected at Ascension Island, U.K. during 2001. These data files normally log an entire UTC day, but this example has been shortened and begins at 2247 UTC, or 80280 seconds and ends four minutes later. PRN (satellite) number 6 is currently being scintillated. The S_4 is 0.680 at 80820, rising as high as 0.87 two minutes later, before being dropped for a minute – note PRN 6 is missing at 81000, only to return a minute later. At 81060 PRN 24 is now reporting an S_4 of 9.00. Note in the preamble “9.99=bad data”. This is an error; “bad data” was actually assigned 9.00. See Section 3.2 for more information.

4; Number of Header Records

 ; GPS Computed Ephemeris for 1-minute Data files

 ; 8 Records per 1-minute data record

 -7.94 ; Station Latitude

 -14.39 ; Station Longitude

9; Number of Records per Measurement Set 1)

Yr,dy,sec,nprn,iprn(nprn) (i2,1x,i3,1x,i6,1x,i4,etc) 2) s4

scintillation indices (9.99 = bad data) 3) nprn repeats of

satellite latitude (deg) (f9.3) 4) nprn repeats of satellite

altitude (emr) (f9.4) 5) nprn repeats of satellite longitude (deg)

(f9.3) 6) nprn repeats of azimuth angle (deg) (f9.3) 7) nprn

repeats of elevation angle (deg) (f9.3) 8) nprn repeats of 300 km

pp latitude (deg) (f9.3) 9) nprn repeats of 300 km pp longitude

(deg) (f9.3)

⋮

(A.1)

1 89 80820 6 4 2 26 7 8 27

0.680 0.030 0.040 0.030 0.020 0.160

10.244	-41.176	-11.612	-45.504	10.228	30.778
4.192	4.128	4.121	4.120	4.175	4.230
-12.214	8.724	-74.462	-21.075	2.423	16.826
6.830	152.030	261.172	187.615	42.932	36.203
66.152	40.301	17.395	41.527	58.006	29.161
-6.814	-10.543	-8.941	-10.746	-6.770	-4.440
-14.254	-12.983	-21.304	-14.772	-13.295	-11.827
1	89	80880	6	4	2 26 7 8 27
0.850	0.030	0.050	0.030	0.010	0.220
9.837	-40.862	-11.193	-45.785	10.633	31.132
4.191	4.128	4.120	4.120	4.175	4.230
-12.177	9.008	-74.409	-20.713	2.470	16.964
7.105	151.453	261.661	187.128	42.353	36.000
66.664	40.438	17.431	41.251	57.594	28.775
-6.841	-10.517	-8.882	-10.776	-6.741	-4.382
-14.252	-12.963	-21.301	-14.751	-13.290	-11.804
1	89	80940	6	4	2 26 7 8 27
0.870	0.020	0.040	0.010	0.020	0.200
9.429	-40.545	-10.775	-46.064	11.039	31.485
4.191	4.129	4.120	4.120	4.175	4.230
-12.141	9.287	-74.357	-20.344	2.517	17.106
7.391	150.874	262.151	186.644	41.790	35.801
67.177	40.574	17.463	40.976	57.178	28.389
-6.869	-10.491	-8.822	-10.805	-6.711	-4.322
-14.250	-12.944	-21.298	-14.730	-13.285	-11.780
1	89	81000	5	2	26 7 8 27
0.010	0.040	0.030	0.040	0.200	
-40.226	-10.356	-46.339	11.444	31.837	
4.130	4.120	4.120	4.174	4.230	

	9.561	-74.306	-19.969	2.565	17.251	
	150.293	262.641	186.163	41.242	35.606	
	40.709	17.493	40.701	56.761	28.002	
	-10.465	-8.763	-10.834	-6.681	-4.262	
	-12.924	-21.296	-14.708	-13.280	-11.756	
1	89	81060	6	2	26	7 8 27 24
	0.010	0.050	0.030	0.040	0.170	9.000
	-39.906	-9.937	-46.611	11.849	32.188	36.601
	4.131	4.120	4.120	4.174	4.230	4.195
	9.829	-74.256	-19.587	2.614	17.399	-34.870
	149.710	263.133	185.684	40.708	35.416	337.977
	40.845	17.520	40.427	56.340	27.616	29.518
	-10.438	-8.703	-10.863	-6.651	-4.200	-3.976
	-12.905	-21.294	-14.686	-13.274	-11.730	-15.995

Appendix B. Z-Test on Means

Results of Z-Test on mean differences between imputed and raw values for each week at a given location for a given year are shown in Table 1. The first two columns show the percentile and S_4 level compared. The *week* column refers to the week in which the highest mean was recorded using the *original imputation scheme*. Lower and upper 95% confidence-interval limits for the mean difference between imputed and raw values are shown as *CI min* and *CI max*. The *Original Scheme* refers to the results obtained using the original imputation scheme while the *Modified Scheme* refers to the results from the imputation scheme with the addition of a 0.3 S_4 threshold and the expansion of the duration limit to 20 min. In general the confidence interval limits increased for Anomaly Crest stations (Ascension and Parepare) using the modified imputation scheme, particularly during the solar maximum. At the stations closer to the geomagnetic equator (Ancon and Marak Parak), confidence-interval limits decreased or remained the same. Although not shown, the weeks for which the highest mean was recorded using the modified imputation scheme tended to be better clustered around the equinoxes.

Table 1: Results of Z-Test on mean differences between imputed and raw values for each week at a given location for a given year. The first two columns show the percentile and S_4 level compared. The *week* column refers to the week in which the highest mean was recorded using the *original imputation scheme*. Lower and upper 95% confidence-interval limits for the mean difference between imputed and raw values are shown as *CI min* and *CI max*. The *Original Scheme* refers to the results obtained using the original imputation scheme while the *Modified Scheme* refers to the results from the imputation scheme with the addition of a 0.3 S_4 threshold and the expansion of the duration limit to 20 min.

Percentile	S_4	Week	CI Min	CI Max	CI Min	CI Max
			Original Scheme	Modified Scheme		
Ascension 2001						
50	0.3	47	0.039	0.041	0.051	0.054
50	0.5	46	0.051	0.055	0.061	0.065
50	0.8	46	0.055	0.06	0.081	0.09
75	0.3	45	0.044	0.046	0.051	0.054
75	0.5	43	0.065	0.068	0.068	0.071
75	0.8	10	0.086	0.093	0.086	0.093
95	0.3	10	0.048	0.05	0.048	0.05
95	0.5	10	0.05	0.056	0.05	0.056
95	0.8	47	0.062	0.064	0.072	0.079

Continued on next page

Table 1 – continued from previous page

Percentile	S_4	Week	CI Min	CI Max	CI Min	CI Max
			Original Scheme		Modified Scheme	
Ascension 2004						
50	0.3	45	0.06	0.107	0.052	0.082
50	0.5	45	0.045	0.066	0.02	0.023
50	0.8	3	0.007	0.008	0.026	0.031
75	0.3	45	0.099	0.113	0.101	0.126
75	0.5	46	0.091	0.109	0.11	0.145
75	0.8	46	0.101	0.122	0.101	0.122
95	0.3	46	0.081	0.097	0.121	0.279
95	0.5	41	0.099	0.148	0.116	0.35
95	0.8	45	0.093	0.129	0.103	0.519
Ancon 1998						
50	0.3	7	0.002	0.002	0.0	0.0
50	0.5	1	0.0	0.0	0.0	0.0
50	0.8	1	0.0	0.0	0.0	0.0
75	0.3	35	0.022	0.028	0.022	0.028
75	0.5	35	0.022	0.028	0.0	0.0
75	0.8	35	0.022	0.028	0.0	0.0
95	0.3	45	0.051	0.104	0.007	0.007
95	0.5	35	0.058	0.11	0.013	0.015
95	0.8	35	0.058	0.11	0.013	0.015

Continued on next page

Table 1 – continued from previous page

Percentile	S_4	Week	CI Min	CI Max	CI Min	CI Max
			Original Scheme		Modified Scheme	
Ancon 2001						
50	0.3	49	0.016	0.017	0.006	0.007
50	0.5	51	0.009	0.01	0.005	0.006
50	0.8	1	0.0	0.0	0.0	0.0
75	0.3	6	0.011	0.012	0.007	0.007
75	0.5	46	0.015	0.016	0.017	0.019
75	0.8	51	0.01	0.011	0.01	0.011
95	0.3	20	0.074	0.124	0.006	0.007
95	0.5	20	0.061	0.137	0.011	0.012
95	0.8	20	0.061	0.137	0.018	0.02
Parepare 1998						
50	0.3	36	0.005	0.006	0.005	0.006
50	0.5	40	0.02	0.022	0.02	0.022
50	0.8	22	0.006	0.007	0.006	0.007
75	0.3	36	0.014	0.015	0.014	0.015
75	0.5	36	0.019	0.02	0.019	0.02
75	0.8	36	0.022	0.024	0.021	0.023
95	0.3	42	0.025	0.027	0.015	0.016
95	0.5	46	0.018	0.02	0.011	0.012
95	0.8	36	0.034	0.037	0.033	0.035

Continued on next page

Table 1 – continued from previous page

Percentile	S_4	Week	CI Min	CI Max	CI Min	CI Max
			Original Scheme		Modified Scheme	
Parepare 2000						
50	0.3	13	0.029	0.03	0.034	0.036
50	0.5	13	0.022	0.023	0.027	0.029
50	0.8	13	0.023	0.025	0.035	0.039
75	0.3	38	0.024	0.025	0.031	0.033
75	0.5	38	0.036	0.038	0.04	0.043
75	0.8	13	0.053	0.058	0.068	0.074
95	0.3	47	0.024	0.026	0.041	0.056
95	0.5	10	0.048	0.052	0.049	0.053
95	0.8	13	0.055	0.059	0.068	0.074
Marak Parak 2001						
50	0.3	15	0.005	0.006	0.004	0.004
50	0.5	10	0.006	0.007	0.006	0.007
50	0.8	1	0.0	0.0	0.0	0.0
75	0.3	25	0.005	0.005	0.003	0.003
75	0.5	12	0.01	0.011	0.006	0.006
75	0.8	39	0.005	0.005	0.005	0.005
95	0.3	22	0.011	0.013	0.007	0.007
95	0.5	5	0.04	0.043	0.008	0.009
95	0.8	10	0.044	0.047	0.032	0.035

Continued on next page

Table 1 – continued from previous page

Percentile	S_4	Week	CI Min	CI Max	CI Min	CI Max
				Original Scheme	Modified Scheme	
Marak Parak 1998						
50	0.3	14	0.005	0.005	0.0	0.0
50	0.5	16	0.006	0.006	0.0	0.0
50	0.8	16	0.006	0.006	0.0	0.0
75	0.3	17	0.006	0.006	0.0	0.0
75	0.5	17	0.005	0.005	0.0	0.0
75	0.8	12	0.007	0.007	0.0	0.0
95	0.3	11	0.013	0.013	0.002	0.003
95	0.5	31	0.017	0.018	0.003	0.003
95	0.8	32	0.021	0.023	0.001	0.001

Bibliography

- Beach, T. L., T. Pedersen, M. J. Starks, and S.-Y. Su (2002), Estimation the amplitude scintillation index from sparsely sampled phase screen data, *Radio Science*, 39, RS5001, doi: 10.1029/2002RS002792.
- Cervera, M. A., R. M. Thomas, K. M. Groves, A. G. Ramli, and Effendy (2001), Validation of wbmod in the southeast asia region, *Radio Science*, 36(6), 1559–1572.
- Dandekar, B. S., and K. M. Groves (2004), Using ionospheric scintillation observations for studying the morphology of equatorial ionospheric bubbles, *Radio Science*, 39(3), doi: 10.1029/2003RS003020.
- Datta-Barua, S., P. H. Doherty, S. H. Delay, T. Dehel, and J. A. Klobuchar (2003), Ionospheric scintillation effects on single and dual frequency gps positioning, in *Proceedings of ION GPS/GNSS 2003*, Institute of Navigation.
- Davies, K. (1990), *Ionospheric Radio*, 590 pp., Peter Peregrinus Ltd, London.
- de La Beaujardiere, O., et al. (2004), C/nofs: a mission to forecast scintillations, *Journal of Atmospheric and Solar Terrestrial Physics*, 66(17), 1573–1591.
- Dempster, A. (2006), Dilution of precision in angle-of-arrival positioning systems, *Electronics Letters*, 42, 291–292, doi: 10.1049/el:20064410.
- Dierendonck, V., Q. Hua, P. Fenton, and J. Klobuchar (1996), Commercial ionospheric scintillation monitoring receiver development and test results, in *Proceedings of the 52nd Annual Meeting of the Institute of Navigation*, Institute of Navigation.
- Evans, C. (2005), Ionospheric scintillation effects on gps performance and weapon’s effectiveness, in *18th International Technical Meeting, Institute of Navigation; ION GNSS 2005*, pp. 690–696, Institute of Navigation, Fairfax, VA.
- Fremouw, E. J., R. C. Livingston, and D. A. Miller (1980), On the statistics of scintillating signals, *Journal of Atmospheric and Terrestrial Physics*, 42, 717–731.
- Groves, K., S. Basu, G. Bishop, E. Weber, and J.M.Quinn (1996), Ionospheric effects on gps navigation, in *Proceedings of the 52nd Annual Meeting "Navigation*

- Technology for the 3rd Millenium*, pp. 583–591, Institute of Navigation, Institute of Navigation, Fairfax VA.
- Groves, K. M., et al. (1997), Equatorial scintillation and systems support, *Radio Science*, 32(5), 2047–2064.
- Hofmann-Wellenhof, B., H. Lichtenegger, and J. Collins (2001), *Global Positioning System : theory and practice*, 382 pp., Springer-Verlag, New York, b. Hofmann-Wellenhof, H. Lichtenegger, and J. Collins.; Includes bibliographical references (p. [355]-370) and index.
- Immel, T. J., S. B. Mende, H. U. Frey, L. M. Peticolas, and E. Sagawa (2003), Determination of low latitude plasma drift speeds from fuv images, *Geophysical Research Letters*, 30, 7–1.
- Kelley, M. C. (1989), *The Earth's Ionosphere, Plasma Physics and Electrodynamics*, Academic Press, San Diego, CA.
- Knight, M., M. Cervera, and A. Finn (1999), A comparison of predicted and measured gps performance in an ionospheric scintillation environment., in *Proceedings of ION GPS-99, 12th International Technical Meeting of the Satellite Division of the Institute of Navigation*, pp. 1437–1450, Institute of Navigation, Institute of Navigation, Fairfax VA.
- Knight, M. F. (2000), Ionospheric scintillation effects on global positioning system receivers, Phd, University of Adelaide, Dept. of Electrical and Electronic Engineering.
- Little, R. J., and D. B. Rubin (2002), *Statistical Analysis with Missing Data*, 2nd. ed., Wiley-Interscience.
- Milner, B. R. (2002), Evaluation of environmental effects on gps navigation systems: Scintillation data collection, *Tech. rep.*, MISSION RESEARCH CORP SANTA BARBARA CA.

- Parkinson, B. W., J. J. Spilker, P. Axelrad, and P. Enge (1996), *The global positioning system : theory and applications*, Progress in astronautics and aeronautics, American Institute of Aeronautics and Astronautics, Washington, DC.
- Rino, C. L. (1979b), A power law phase screen model for ionospheric scintillation, 2. strong scatter, *Radio Science*, 14.
- Schafer, J. (1997), *Analysis of Incomplete Multivariate Data*, Monographs on Statistics and Applied Probability 72, Chapman & Hall.
- Schunk, R. W., and A. F. Nagy (2000), *Ionospheres: Physics, Plasma Physics, and Chemistry*, Cambridge Atmosphere and Space Science Series, Cambridge University Press, Cambridge, UK.
- Thomas, R. M., M. A. Cervera, A. G. Ramli, Effendy, P. Tutarong, K. M. Groves, and P. J. Wilkinson (2004), Seasonal modulation of gps performance due to equatorial scintillation, *Geophysical Research Letters*, 31(18), doi: 10.1029/2004GL020581.
- Thomas, R. M., et al. (2001), A regional gps receiver network for monitoring equatorial scintillation and total electron content, *Radio Science*, 36(6), 1545–1557.
- Wheelon, A. D. (2003), *Electromagnetic Scintillation*, vol. II. Weak Scattering, Cambridge University Press.
- Wilks, D. S. (1995), *Statistical Methods in the Atmospheric Sciences: an introduction*, 2nd. ed., Academic Press, San Diego.
- Woodman, R. F., and E. Kudeki (1984), A causal relationship between lightning and explosive spread f, *Geophysical Research Letters*, 11, 1165–1167.

Vita

SMSgt Robert A. Steenburgh is a twenty one year veteran of the United States Air Force. He was born in Columbus, Ohio, graduated from Gahanna Lincoln High School and by 1985 had entered the Air Force as a weather observer. After graduating with honors from weather observing school at Chanute Air Force Base, Illinois, SMSgt Steenburgh was selected to attend the weather forecasting course as part of a pilot “fast track” program for Air Force weather personnel. At his first assignment he earned an Associate of Applied Science in Weather Technology from the Community College of the Air Force. He was also selected as the Air Weather Service Airman of the Year for 1987. He eventually returned to Chanute as a forecasting instructor. He was selected to attend the National Weather Services Doppler Weather Radar (NEXRAD) course in Norman Oklahoma. He subsequently taught meteorological radar theory and operations and helped develop the Department of Defense’s Doppler Weather Radar resident courses.

In 1998 SMSgt Steenburgh completed a B.Sc. in meteorology at North Carolina State University, graduating Summa Cum Laude at the top of his class in Marine Earth and Atmospheric Sciences. He earned a scholarship and incentive award from the local American Meteorological Society and was elected to membership in Phi Beta Kappa, the nations oldest undergraduate honor society. SMSgt Steenburgh went on to play a key role in the development of training materials for the modernized and restructured Air Force Weather community.

In 2005, SMSgt Steenburgh was selected as the first enlisted Air Force member to study physics at the Air Force Institute of Technology.

SMSgt Steenburgh has been a fellow of the Royal Meteorological Society (U.K.) since 1988 and a member of the American Meteorological Society since 1995. His military decorations include 3 Meritorious Service Medals and an Army Commendation Medal.

Permanent address: 2950 Hobson Way
Air Force Institute of Technology
Wright-Patterson AFB, OH 45433

REPORT DOCUMENTATION PAGE					<i>Form Approved OMB No. 0704-0188</i>	
<p>The public reporting burden for this collection of information is estimated to average 1 hour per response, including the time for reviewing instructions, searching existing data sources, gathering and maintaining the data needed, and completing and reviewing the collection of information. Send comments regarding this burden estimate or any other aspect of this collection of information, including suggestions for reducing the burden, to Department of Defense, Washington Headquarters Services, Directorate for Information Operations and Reports (0704-0188), 1215 Jefferson Davis Highway, Suite 1204, Arlington, VA 22202-4302. Respondents should be aware that notwithstanding any other provision of law, no person shall be subject to any penalty for failing to comply with a collection of information if it does not display a currently valid OMB control number.</p> <p>PLEASE DO NOT RETURN YOUR FORM TO THE ABOVE ADDRESS.</p>						
1. REPORT DATE (DD-MM-YYYY)		2. REPORT TYPE			3. DATES COVERED (From - To)	
4. TITLE AND SUBTITLE				5a. CONTRACT NUMBER		
				5b. GRANT NUMBER		
				5c. PROGRAM ELEMENT NUMBER		
6. AUTHOR(S)				5d. PROJECT NUMBER		
				5e. TASK NUMBER		
				5f. WORK UNIT NUMBER		
7. PERFORMING ORGANIZATION NAME(S) AND ADDRESS(ES)					8. PERFORMING ORGANIZATION REPORT NUMBER	
9. SPONSORING/MONITORING AGENCY NAME(S) AND ADDRESS(ES)					10. SPONSOR/MONITOR'S ACRONYM(S)	
					11. SPONSOR/MONITOR'S REPORT NUMBER(S)	
12. DISTRIBUTION/AVAILABILITY STATEMENT						
13. SUPPLEMENTARY NOTES						
14. ABSTRACT						
15. SUBJECT TERMS						
16. SECURITY CLASSIFICATION OF:			17. LIMITATION OF ABSTRACT	18. NUMBER OF PAGES	19a. NAME OF RESPONSIBLE PERSON	
a. REPORT	b. ABSTRACT	c. THIS PAGE			19b. TELEPHONE NUMBER (Include area code)	